

One-dimensional delayed-detonation models of Type Ia supernovae: Confrontation to observations at bolometric maximum

Stéphane Blondin,^{1,2*} Luc Dessart,^{1,3} D. John Hillier,⁴ and Alexei M. Khokhlov⁵

¹*Aix Marseille Université, CNRS, LAM (Laboratoire d'Astrophysique de Marseille) UMR 7326, 13388, Marseille, France.*

²*Centre de Physique des Particules de Marseille (CPPM), Aix Marseille Université, CNRS/IN2P3, Marseille, France.*

³*TAPIR, Mail code 350-17, California Institute of Technology, Pasadena, CA 91125, USA.*

⁴*Department of Physics and Astronomy, University of Pittsburgh, Pittsburgh, PA 15260, USA.*

⁵*Department of Astronomy & Astrophysics, the Enrico Fermi Institute, and the Computation Institute, The University of Chicago, Chicago, IL 60637, USA.*

Accepted 2012 November 23. Received 2012 November 23; in original form 2012 October 15

ABSTRACT

The delayed-detonation explosion mechanism applied to a Chandrasekhar-mass white dwarf offers a very attractive model to explain the inferred characteristics of Type Ia supernovae (SNe Ia). The resulting ejecta are chemically stratified, have the same mass and roughly the same asymptotic kinetic energy, but exhibit a range in ^{56}Ni mass. We investigate the contemporaneous photometric and spectroscopic properties of a sequence of delayed-detonation models, characterized by ^{56}Ni masses between 0.18 and 0.81 M_{\odot} . Starting at 1 d after explosion, we perform the full non-LTE, time-dependent radiative transfer with the code CMFGEN, with an accurate treatment of line blanketing, and compare our results to SNe Ia at bolometric maximum. Despite the 1D treatment, our approach delivers an excellent agreement to observations. We recover the range of SN Ia luminosities, colours, and spectral characteristics from the near-UV to 1 μm , for standard as well as low-luminosity 91bg-like SNe Ia. Our models predict an increase in rise time to peak with increasing ^{56}Ni mass, from ~ 15 to ~ 21 d, yield peak bolometric luminosities that match Arnett's rule to within 10 % and reproduce the much smaller scatter in near-IR magnitudes compared to the optical. We reproduce the morphology of individual spectral features, the stiff dependence of the $\mathcal{R}(\text{Si})$ spectroscopic ratio on ^{56}Ni mass, and the onset of blanketing from Ti II/Sc II in low-luminosity SNe Ia with a ^{56}Ni mass $\lesssim 0.3 M_{\odot}$. We find that ionization effects, which often dominate over abundance variations, can produce high-velocity features in Ca II lines, even in 1D. Distinguishing between different SN Ia explosion mechanisms is a considerable challenge but the results presented here provide additional support to the viability of the delayed-detonation model.

Key words: radiative transfer – supernovae: general

1 INTRODUCTION

All models for Type Ia supernovae (SNe Ia) involve the thermonuclear disruption of a C/O white dwarf (WD) star (Hoyle & Fowler 1960). Fusion of ^{12}C and ^{16}O to iron-peak elements provides the energy to unbind the star and accelerate the ejecta to expansion velocities on the order of 10000 km s^{-1} , while synthesizing $\lesssim 1 M_{\odot}$ of ^{56}Ni to power the subsequent light curve (Colgate & McKee 1969).

Nuclear combustion of C and O requires a large temperature ($\sim 10^9 \text{ K}$) in the progenitor star. At present, these conditions seem to be met when the WD mass approaches the Chandrasekhar mass, $M_{\text{Ch}} \approx 1.4 M_{\odot}$, through accretion of material from a companion star (the so-called single-degenerate scenario; Whelan & Iben 1973). Alternatively, combustion may be initiated when two C/O

WDs coalesce (the double-degenerate scenario; Iben & Tutukov 1984; Webbink 1984), in which case the total mass of the system can differ significantly from M_{Ch} . While the single-degenerate scenario provides a natural explanation for the apparent homogeneity of the SN Ia class, recent simulations have shown that violent WD mergers are compatible with both sub-luminous (Pakmor et al. 2010) and normal (Pakmor et al. 2012) SNe Ia. It is thus not clear today whether the Chandrasekhar mass represents a fundamental quantity for SNe Ia.

In addition to multiple progenitor channels, several explosion mechanisms have been proposed. The propagation of the burning front can proceed either sub-sonically (deflagration), or super-sonically (detonation). Pure detonations of C/O WDs (e.g., Arnett 1969) burn the entire star to nuclear statistical equilibrium and fail to synthesize the intermediate-mass elements (IMEs) at high velocities needed to reproduce SN Ia spectra (see, e.g., Branch et al. 1982). Pure deflagrations (e.g., Nomoto, Sugimoto & Neo 1976)

* E-mail: stephane.blondin@oamp.fr

yield copious amounts of IMEs but correspond to less energetic explosions, with ^{56}Ni masses typically $\lesssim 0.4 M_{\odot}$ (see, e.g., Travaglio et al. 2004), and are thus considered a feasible mechanism only for the least luminous events. More importantly, significant amounts of unburnt C/O are expected to be mixed inwards to the WD centre (see, e.g., Gamezo et al. 2003), leading to the firm prediction of conspicuous lines of O I and C I at nebular times that have never been observed (Kozma et al. 2005).

To overcome the shortcomings of both explosion mechanisms, Khokhlov (1991) proposed the delayed-detonation model in which the explosion of a Chandrasekhar-mass C/O WD begins as a subsonic deflagration near its centre and then switches to a supersonic detonation wave at some density, ρ_{tr} , via a deflagration-to-detonation transition (or DDT). The initial deflagration pre-expands the WD and creates low-density conditions required for the production of intermediate mass elements. The ensuing detonation incinerates the remaining unburnt matter. By tuning ρ_{tr} and the deflagration speed, one can synthesize varying amounts of ^{56}Ni and hence account for the observed variation in SN Ia peak luminosity, as well as reproduce the correct stratification of chemical elements in the ejecta inferred from spectroscopic observations. Additional variations in peak luminosity can be induced by varying the C/O ratio and central density of the progenitor WD star (Höflich et al. 2010).

The delayed-detonation model has been successfully tested against SN Ia observations in its 1D (e.g., Höflich, Khokhlov & Wheeler 1995) and multi-D (e.g., Kasen, Röpke & Woosley 2009) versions. It also appears to be consistent with observations of supernova remnants (Badenes et al. 2006, 2008; Fesen et al. 2007). Using a grid of 130 parameterized one-dimensional models, Woosley et al. (2007) studied the ejecta properties necessary to reproduce the fundamental properties of SN Ia light curves, and in particular the width-luminosity relation (Pskovskii 1977; Phillips 1993). They found a good agreement for ejecta with a total burnt mass of $\sim 1.1 M_{\odot}$ (leading to comparable asymptotic kinetic energies in such models), provided the inner layers were strongly mixed, and highlight the adequacy of the delayed-detonation scenario in fulfilling these requirements. However, despite a significant effort in three-dimensional simulations (e.g., Gamezo, Khokhlov & Oran 2005; Röpke & Niemeyer 2007), it is still unclear what may cause strong variations in transition density in the DDT mechanism. Moreover, the lack of unburnt carbon in delayed-detonation models is in conflict with observations of C II 6580 Å absorption in $\sim 30\%$ of SNe Ia with pre-maximum spectra (Parrent et al. 2011; Thomas et al. 2011; Folatelli et al. 2012; Silverman & Filippenko 2012).

Differentiating between these various models requires detailed radiative transfer simulations to match the observed evolution of SN Ia light curves and spectra from early to late times. At present, the observed properties of normal SNe Ia can be reproduced with detonations in single sub- M_{Ch} WDs (Sim et al. 2010) and super- M_{Ch} double-WD mergers (Röpke et al. 2012), in addition to the more conventional Chandrasekhar-mass delayed-detonation model. This may mean that observational differences between these models are too small, or that uncertainties in the modeling approach are too large.

Radiative-transfer modeling of SN Ia ejecta is complicated by the dominance of line opacity (Höflich, Müller & Khokhlov 1993; Pinto & Eastman 2000b), with a mixed absorptive/scattering character that is often enforced, particularly in Monte-Carlo codes (see, e.g. Mazzali & Lucy 1993; Kasen, Thomas & Nugent 2006; Sim 2007), rather than computed directly as part of a

non-Local-Thermodynamic-Equilibrium (non-LTE) solution. Other approaches treat some species in full non-LTE, while others are treated in LTE (e.g., Höflich, Wheeler & Thielemann 1998; Baron et al. 2012). Neglecting time-dependent effects in the radiation transport, which are known to be important (see Höflich & Khokhlov 1996; Pinto & Eastman 2000b; Dessart & Hillier 2010; Jack, Hauschildt & Baron 2009; Hillier & Dessart 2012), numerous studies at bolometric maximum (and sometimes even later) impose a diffusive inner boundary, even though some spectral regions are no longer optically thick. This causes a systematic flux excess in the red, i.e., photons erroneously injected at the inner diffusive boundary fail to thermalize and directly escape the ejecta (e.g., Mazzali et al. 2008). The low densities and strong radiation field in SNe Ia is expected to drive level populations out of LTE, indicating the need for a full non-LTE treatment (Baron et al. 1996; Dessart et al., in prep.).

As part of a new and independent effort, we apply the CM-FGEN code (Hillier & Miller 1998; Hillier & Dessart 2012) to the Chandrasekhar-mass delayed-detonation model of SNe Ia. CM-FGEN is a 1D, non-LTE, time-dependent, radiative-transfer tool that allows for explicit treatment of non-thermal processes and non-local energy deposition (see Hillier & Dessart 2012 for a full description of the code in the context of SN calculations). In this paper we focus on the photometric and spectroscopic properties of delayed-detonation models at bolometric maximum, to study how well this explosion mechanism can predict the observed diversity of SNe Ia at that well-defined time.

In section 2 we present our grid of delayed-detonation models and radiative transfer modeling. In Sect. 3 we present our overall strategy for comparing synthetic light curves and spectra. We then discuss the photometric (Sect. 4) and spectroscopic (Sect. 5) properties at bolometric maximum. We discuss comparisons to individual SN Ia observations in Sect. 6. Discussion and conclusions follow in Sect. 7.

2 NUMERICAL SETUP

2.1 Delayed-detonation models

A grid of one-dimensional delayed-detonation models was calculated following the method described in Khokhlov (1991). The starting point for all models is a Chandrasekhar-mass WD star ($1.41 M_{\odot}$) with a central density of $2.6 \times 10^9 \text{ g cm}^{-3}$, composed of equal mass fractions of ^{12}C and ^{16}O ($X \approx 0.5$) with traces of ^{22}Ne ($X \approx 1.4 \times 10^{-2}$) and solar abundances for all other elements (Anders & Grevesse 1989). The explosion hydrodynamics is described by the reactive flow Euler equations of fluid dynamics which are solved with a one-dimensional Lagrangian hydrodynamics code. During the explosion, nuclear energy release and neutronization of matter were described using a five-equation reaction scheme for ^{12}C concentration, electron and mean ion mole fractions, nuclear binding energy, and the nuclear statistic equilibrium (NSE) progress variable. The reaction scheme takes into account the energy release during the major stages of explosive carbon-oxygen burning: (1) burning of carbon to oxygen, neon, magnesium and silicon, (2) burning of oxygen and establishment of nuclear quasi-equilibrium in Si-group nuclei, and finally (3) the onset of NSE during which the Si-group elements are transformed into iron-peak nuclei. The scheme takes into account neutronization and neutrino energy losses due to electron captures on iron-group nuclei. The neutronization rates were updated according to Seitzzahl et al. (2009).

Table 1. Delayed-detonation model parameters and nucleosynthetic yields for selected species.

Model	ρ_{tr} [g cm ⁻³]	E_{kin} [B]	$v(^{56}\text{Ni})$ [km s ⁻¹]	$M(^{56}\text{Ni})$ [M _⊙]	$M(\text{Ni})$ [M _⊙]	$M(\text{Co})$ [M _⊙]	$M(\text{Fe})$ [M _⊙]	$M(\text{Ti})$ [M _⊙]	$M(\text{Ca})$ [M _⊙]	$M(\text{S})$ [M _⊙]	$M(\text{Si})$ [M _⊙]	$M(\text{Mg})$ [M _⊙]	$M(\text{Na})$ [M _⊙]	$M(\text{O})$ [M _⊙]	$M(\text{C})$ [M _⊙]
DDC0	3.5(7)	1.564	1.31(4)	0.805	0.857	1.15(-2)	0.160	1.19(-4)	2.62(-2)	0.101	0.160	3.51(-3)	5.88(-6)	5.29(-2)	1.18(-3)
DDC6	2.7(7)	1.503	1.21(4)	0.727	0.768	9.10(-3)	0.142	1.21(-4)	3.06(-2)	0.125	0.201	7.18(-3)	9.66(-6)	8.42(-2)	1.76(-3)
DDC10	2.3(7)	1.485	1.16(4)	0.650	0.689	8.36(-3)	0.137	1.24(-4)	3.68(-2)	0.149	0.234	9.55(-3)	1.20(-5)	9.67(-2)	2.11(-3)
DDC15	1.8(7)	1.468	1.12(4)	0.558	0.596	7.87(-3)	0.135	1.25(-4)	4.17(-2)	0.177	0.277	1.14(-2)	1.63(-5)	0.107	2.69(-3)
DDC17	1.6(7)	1.410	1.09(4)	0.458	0.495	7.24(-3)	0.131	1.25(-4)	4.45(-2)	0.200	0.314	1.65(-2)	2.43(-5)	0.139	3.77(-3)
DDC20	1.3(7)	1.382	1.04(4)	0.344	0.380	6.43(-3)	0.126	1.25(-4)	4.53(-2)	0.233	0.374	1.95(-2)	3.40(-5)	0.157	5.05(-3)
DDC22	1.1(7)	1.301	9.85(3)	0.236	0.271	5.52(-3)	0.120	1.24(-4)	4.04(-2)	0.255	0.432	2.45(-2)	6.07(-5)	0.186	8.14(-3)
DDC25	8.0(6)	1.177	8.36(3)	0.180	0.215	4.37(-3)	0.111	1.25(-4)	2.34(-2)	0.230	0.458	3.33(-2)	1.46(-4)	0.248	2.07(-2)

Notes: Numbers in parenthesis correspond to powers of ten. The ratio of the deflagration velocity to the local sound speed ahead of the flame is $\alpha = 0.03$ for all models; ρ_{tr} is the transition density at which the deflagration is artificially turned into a detonation; E_{kin} is the asymptotic kinetic energy (units: 1B \equiv 1Bethe = 10⁵¹ erg); $v(^{56}\text{Ni})$ is the velocity of the ejecta shell that bounds 99% of the total ⁵⁶Ni mass (see Sect. 2.1 for a discussion).

The equation of state includes contributions from electrons and positrons with an arbitrary degree of degeneracy and relativity, ideal ions, and equilibrium radiation. Screening of the ¹²C+¹²C nuclear reaction is taken into account but Coulomb corrections to the equation of state are ignored (see Bravo & García-Senz 1999). They change the relation between the initial central density and the WD mass by ~ 2 –3% but do not noticeably affect the explosion predictions. The approximate kinetic scheme neglects differences between the quasi-equilibrium energy release in Si-group elements and the NSE energy release in Fe-peak elements and may overestimate the energy generation rate during oxygen burning to silicon by up to $\sim 20\%$ as compared to detailed nuclear kinetics.

The initial WD is assumed to be in hydrostatic equilibrium, and the discretized equations of energy and nuclear kinetics are solved simultaneously with high precision to prevent excitation of artificial pulsations during the WD explosion. Weak interaction rates and neutrino energy losses are taken from Seitenzahl et al. (2009). Detailed nucleosynthesis is calculated by post processing temperature, density, and neutronization histories of fluid elements with a detailed reaction network consisting of 144 individual nuclei, ranging from protons and neutrons to zinc. Forward reaction rates, partition functions, and binding energies were taken from Fowler, Woosley & Engelbrecht (1978), Woosley et al. (1978), and F. Thielemann (1993, private communication). Reverse reactions were calculated from the principle of detailed balance.

The deflagration is propagated numerically with a prescribed velocity $D_{\text{def}} = \alpha a_s$ relative to unburnt matter, where $\alpha < 1$ is a constant and a_s is the local sound speed ahead of the deflagration front. We use $\alpha = 0.03$ in the models considered in this paper. The transition to a detonation is artificially triggered by rising D_{def} above the maximum Chapman-Jouguet speed for a steady-state deflagration when the density ahead of the deflagration front reaches a prescribed transition density, ρ_{tr} . This causes the onset of a self-sustained supersonic detonation wave after the accelerated deflagration front propagates ~ 3 –5 computational cells. The calculations are run until 30–60 s past explosion, by which time the ejecta have expanded by two orders of magnitude and are in homologous expansion.

The earlier the transition from a deflagration to a detonation occurs (i.e. the higher the transition density ρ_{tr}), the more efficiently the burning proceeds to large velocities with more ⁵⁶Ni being synthesized at the expense of intermediate-mass elements (Fig. 1). From model DDC0 to DDC25, the velocity of the ejecta shell that bounds 99% of the total ⁵⁶Ni mass drops from

~ 13000 km s⁻¹ to ~ 8000 km s⁻¹, while the mass of synthesized ⁵⁶Ni goes from $\sim 0.81M_{\odot}$ to $\sim 0.18M_{\odot}$ (see Table 1). At the largest velocities one recovers the original composition of the progenitor WD star.

Since the WD is almost entirely consumed in 1D delayed-detonation models (there is at most $\sim 0.02M_{\odot}$ of unburnt carbon for model DDC25), the fraction of primordial C/O not burnt to ⁵⁶Ni is burnt to IMEs, with a comparable nuclear energy release in both cases. This leads to a unique property of the delayed-detonation model, whereby variations in the transition density results in SN Ia explosions with the same ejecta mass and roughly the same asymptotic kinetic energy (E_{kin}), but with varying amounts of ⁵⁶Ni. In our model set, E_{kin} varies by only 50% for a change in ⁵⁶Ni mass by a factor of 4.5.

2.2 Non-LTE time-dependent radiative transfer

Our approach to solve the non-LTE time-dependent radiative-transfer problem for SN ejecta is versatile and generic. It applies irrespective of the SN type and we thus use here the same approach as, e.g., in the recent study of pair-instability SN explosions by Dessart et al. (2012b). The technique is presented in a sequence of papers (Dessart & Hillier 2005, 2008; Li, Hillier & Dessart 2012; Dessart et al. 2012a). A thorough discussion of the application of the code CMFGEN to supernovae has been presented by Hillier & Dessart (2012).

Starting at 1 d after explosion, we simultaneously simulate the evolution of the full ejecta, including the gas thermodynamics state (non-LTE ionization and excitation, and temperature) and the radiation (either trapped or escaping). This evolution is controlled by cooling and heating processes. At early times, cooling stems primarily from expansion, which in SNe Ia corresponds to a factor of 10^{6–7} increase in radius from the original exploding white dwarf to the time of bolometric maximum at ~ 20 d. Heating is dominated in our simulations by the radioactive decay of ⁵⁶Ni and ⁵⁶Co nuclei.

We solve the radiative-transfer problem using a non-LTE treatment. Hence, all atom/ion level populations are determined through a solution of the statistical equilibrium equations, coupled to the gas energy equations and the 0th and 1st moments of the radiative-transfer equation. Level populations are therefore controlled by radiative and collisional rates explicitly (see Hillier & Miller 1998 for details). We do not use the questionable assumption of LTE for the thermodynamical state of the gas, nor the Equivalent-Two-Level-Atom approximation for solving level populations. Together

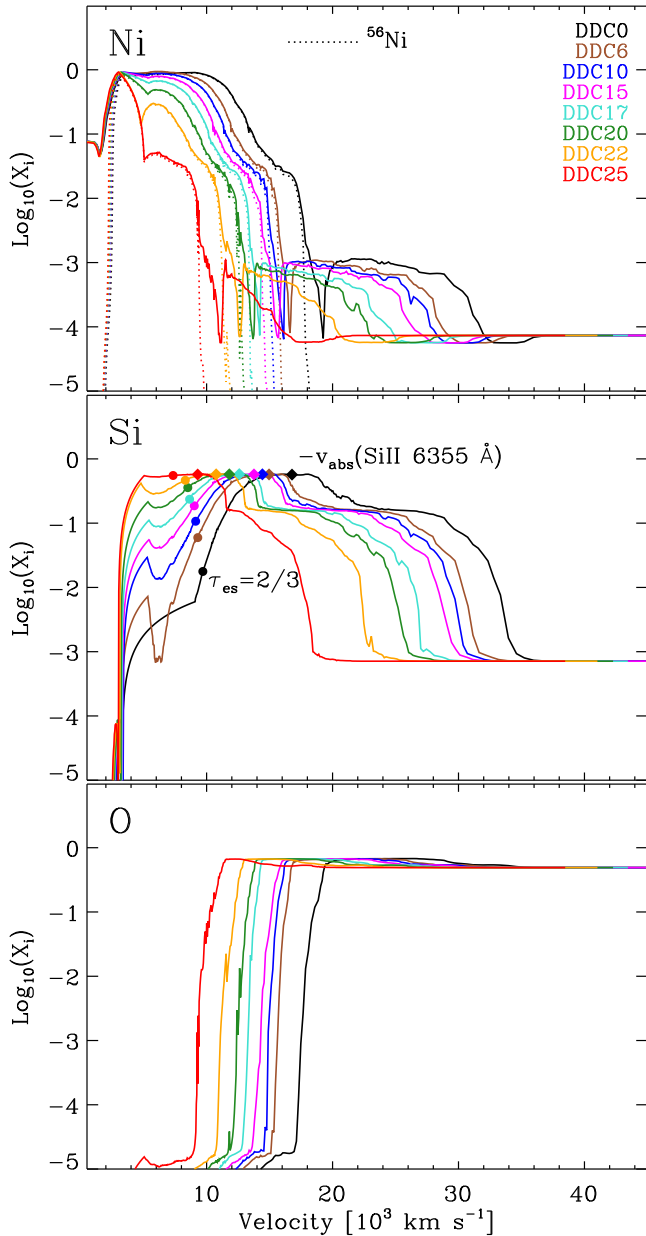


Figure 1. Comparison of the mass fractions of Ni (top; ^{56}Ni shown as dotted lines), Si (middle), and O (bottom) in velocity space for our model set. The drop in ^{56}Ni mass fraction (e.g., at $\sim 5000 \text{ km s}^{-1}$ in model DDC25) corresponds to the ejecta location where the deflagration transitions to a detonation. Note the absence of ^{56}Ni in the inner ejecta layers (up to $v \sim 2000 \text{ km s}^{-1}$) due to rapid electron captures. In the middle panel we overplot the location where the inward-integrated electron scattering optical depth $\tau_{\text{es}} = 2/3$ (dots), as well as minus the velocity at maximum absorption in the Si II 6355 Å line (negative by convention; diamonds).

with charge conservation, this yields a non-LTE ionization. Furthermore, we allow for time dependence both for the radiative transfer, in order to compute accurately the transport of radiation through the ejecta, as well as in the statistical-equilibrium and energy equations, in order to account for the time-dependent effects on the non-LTE ionization/excitation state of the gas (Dessart & Hillier 2008; see also Utrobin & Chugai 2005).

Opacity plays a critical role in SNe Ia. Through its impact on the ejecta optical depth, it controls in part the light-curve

morphology (Arnett 1982; Höflich, Müller & Khokhlov 1993; Pinto & Eastman 2000b). In the spectrum formation region, it modulates the magnitude of line blanketing (Dessart & Hillier 2010; Dessart et al. 2012b), and is thought in SNe Ia to lead to a secondary maximum in near-IR light curves (Kasen 2006). In CMFGEN, we incorporate line blanketing by explicitly treating bound-bound transitions between model atom/ion levels (this is part of the non-LTE solution). Hence, we use no ad-hoc prescription for the thermalization character of the gas, as typically done in the community (sometimes in combination with LTE for the state of the gas). In the present simulations, we adopt a set of model atoms for which we obtain converged results (i.e., increasing further the size of the model atoms alters negligibly the resulting radiation and gas properties) — this required extensive testing, whose results will be presented in a separate paper (Dessart et al., in prep). In practice, we include C I–IV, O I–IV, Ne I–III, Na I, Mg II–III, Al II–III, Si II–IV, S II–IV, Ar I–III, Ca II–IV, Sc II–III, Ti II–III, Cr II–IV, Mn II–III, Fe I–VII, Co II–VII, and Ni II–VII. The number of levels (both super-levels and full levels; see Hillier & Miller 1998 for details) is given in the appendix, in Table A1. The highest ionization stages that are needed to model the transport at early times are no longer needed at bolometric maximum and thus these ions are omitted from that table.

The output of the hydrodynamical calculations at 30–60 s past explosion is evolved to 1 d using a separate program. This program solves the energy equation given by the first law of thermodynamics, assuming the material is radiation dominated (which holds everywhere apart from the ^{56}Ni -deficient higher-density inner ejecta below $\sim 2000 \text{ km s}^{-1}$); we allow for ^{56}Ni decay but neglect the diffusion of the associated heat. Given the high ejecta densities during the first day after explosion, and our focus on maximum-light spectra ~ 20 d later, these approximations are adequate.

We then remap the resulting ejecta at 1 d into CMFGEN. The ejecta, whose velocity ranges from 500 to 45000 km s^{-1} and density from $\sim 3 \times 10^{-9}$ to $\sim 3 \times 10^{-15} \text{ g cm}^{-3}$, are typically resolved with 100–120 radial points, distributed evenly in optical-depth scale to have a minimum of 5–7 points per decade. For the initial relaxation from the hydrodynamical input (see below), we keep the temperature fixed and solve for the full relativistic transfer in non-LTE (Hillier & Dessart 2012). The inner ejecta is very hot at that time (typically 10^5 K in the innermost ^{56}Ni -rich region), while the outer ejecta is at $\lesssim 10^3 \text{ K}$. Since we model the full ejecta, this requires the simultaneous treatment of highly ionized species (which we limit to six-times ionized Fe/Co/Ni and five-times ionized O, for example) and neutral species with C I, O I, or Fe I. To avoid numerical overflow in this initial relaxation at 1 d (see details in Dessart & Hillier 2010), we have to enforce a floor temperature in the outer ejecta of 6000 K — this floor value is reduced to 2000–3000 K in subsequent time steps when we let the temperature vary in the time-dependent calculation. Together with the other approximations used for the evolution of the gas from $\lesssim 100$ s to 1 d, this implies that our simulations need a few time steps to relax from their initial conditions.

We adopt a time increment of 10% of the current time until ~ 21 d past explosion, corresponding to 33 time steps from the initial time at 1 d. Subsequently, we use a fixed 2 d increment to ensure a good time resolution. In the models with a large ^{56}Ni mass, the outer ejecta relaxes to the outward diffusion of heat released at greater depths, as well as radiative and expansion cooling, within a few 0.1 d because of the close proximity of the ^{56}Ni to the outer ejecta. In the models with a low ^{56}Ni mass, this relaxation is slower, and takes ~ 1 –2 d. None of these issues are important for the com-

parison to observations at bolometric maximum, ~ 15 – 21 d after explosion. Probably more relevant than any shortcoming of this initial setup is the neglect of multi-dimensional effects, in particular associated with inward mixing of unburnt C/O and outward mixing of ^{56}Ni (see, e.g., Gamezo, Khokhlov & Oran 2005).

We allow for non-local energy deposition from radioactive decay, using a Monte-Carlo approach for γ -ray transport (Hillier & Dessart 2012). We also treat the non-thermal processes associated with the high-energy electrons produced by Compton scattering and photoelectric absorption of these γ -rays (Li, Hillier & Dessart 2012; Dessart et al. 2012a). These processes are generally unimportant at early times and so we included them starting at ~ 15 d after explosion.

3 STRATEGY

In this study, we adopt a forward-modeling approach. We start with a grid of realistic explosion models and solve the time-dependent radiation-transport problem. An important validation of such delayed-detonation models is through direct confrontation to observations. We do not attempt to model a specific SN — instead we confront each of our models with a large database of SN Ia light curves and spectra. Our goal is to explore how well our range of delayed-detonation models (which span a factor of 4.5 in ^{56}Ni mass) can reproduce the observed range of SN Ia properties, as for example described by the different subclasses proposed by Branch et al. (2006).

All models were evolved from 1 d after explosion until beyond bolometric maximum. Here we focus the discussion exclusively on the time of bolometric maximum, and defer to subsequent papers the study of the rise to peak, the early post-peak evolution and the width-luminosity relation, as well as the nebular phase. The spectra at each time step are integrated over frequency to yield bolometric light curves. We infer the time of peak bolometric luminosity through a 3rd-order polynomial fit to the light curve. The synthetic spectra are interpolated in time to yield maximum-light spectra for all models. Since we simultaneously compute spectra and light curves, we can directly compare SN luminosity and spectroscopic morphology. For educational purposes, we can reveal the direct contributions of individual ions to the total flux by computing the synthetic spectra using the same converged radiative-transfer solution, but ignoring all bound-bound transitions of a given ion in the formal solution of the transfer equation (see Appendix B).

In the next sections, we present the basic properties of our delayed-detonation model series and confront their photometric (Sect. 4) and spectroscopic (Sect. 5) properties to the plethora of publicly-available SN Ia observations. Since the true bolometric luminosity is not known for most SNe Ia, we generate pseudo-bolometric (UVOIR) light curves from *UBVRI* magnitudes for both models and data using the method of Valenti et al. (2008). Observed magnitudes are corrected for extinction (in the MW as well as in the host galaxy) and placed on an absolute scale using the distance moduli inferred for each SN (Sect. 6). We then compare the synthetic and observed peak UVOIR luminosities, the ratio of which is noted Q_{UVOIR} . We also compare the magnitudes and broadband colours at bolometric maximum in various optical and NIR bands. Observed spectra are de-redshifted and de-reddened and scaled to the absolute *V*-band magnitude derived from photometry. To enable a better comparison of individual spectroscopic features, an additional scaling, F_{sc1} , is applied to the data in order to match the mean synthetic flux in the range 4000–6000 Å. In most

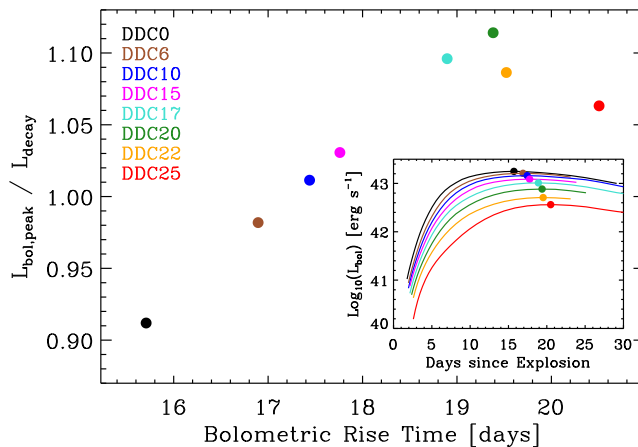


Figure 2. Ratio of the peak bolometric luminosity ($L_{\text{bol,peak}}$) to the instantaneous rate of decay energy (L_{decay}) versus rise time to bolometric maximum for our model set (see also Khokhlov, Müller & Höflich 1993, their Fig. 29). Our results suggest that Arnett’s rule ($L_{\text{bol,peak}}/L_{\text{decay}} = 1$) is accurate to within 10% for such delayed-detonation models. The inset shows the bolometric light curves up until a few days past bolometric maximum (marked with a filled circle).

cases $F_{\text{sc1}} \approx 1$ to within 10%, and in all cases consistent with unity when taking into account errors on the adopted distances. The detailed comparison to individual observations achieving the “best-match” to each of our delayed-detonation models is presented in Sect. 6.

4 PHOTOMETRIC PROPERTIES AT BOLOMETRIC MAXIMUM

The fundamental asset of the delayed-detonation model is its ability to induce a variation in ^{56}Ni , controlled through the deflagration-to-detonation transition density. This introduces diversity in ejecta that have otherwise very similar credentials (mass, kinetic energy, energy lost to unbind the progenitor, energy lost to expansion). It is thus no surprise that this variation in ^{56}Ni drives the main contrast in model results.

The first observable affected by the variation in ^{56}Ni mass is the peak luminosity, which correlates with the heating rate from decay. In the sequence DDC25 to DDC0, the peak bolometric luminosity ranges from $3.64 \times 10^{42} \text{ erg s}^{-1}$ to $1.77 \times 10^{43} \text{ erg s}^{-1}$ (i.e., from $9.5 \times 10^8 L_{\odot}$ to $4.6 \times 10^9 L_{\odot}$). We obtain the following relation for our model set between the peak bolometric luminosity and the ^{56}Ni mass:

$$L_{\text{bol,peak}} \sim 2.21 \times 10^{43} \times \frac{M(^{56}\text{Ni})}{M_{\odot}} \text{ erg s}^{-1}.$$

The degeneracy of progenitor and explosion properties, varying primarily in the amount of heating through decay, is in part the cause of this linear relation to ^{56}Ni mass.

For all models the ratio of the peak bolometric luminosity to the instantaneous rate of decay energy (noted Q_{γ} in Table 2) is within $\sim 10\%$ of unity (Fig. 2), thus supporting the so-called “Arnett rule” (Arnett 1979, 1982). This rule proposes that the light curves of the bolometric luminosity and the instantaneous decay rate should cross around the time of bolometric maximum. At this time, the ejecta Rosseland-mean optical depth in our simulations is a few tens, so that there is still trapped radiation within the SN, making the optical light curve exceed the γ -ray light curve after

Table 2. Various quantities at bolometric maximum characterizing our delayed-detonation model set.

Model	$M(^{56}\text{Ni})$ [M_{\odot}]	t_{rise} [day]	L_{bol} [erg s^{-1}]	Q_{γ}	$B - R$ [mag]	M_{τ} [M_{\odot}]	v_{τ} [km s^{-1}]	T_{τ} [10^4 K]	$X(^{56}\text{Ni})_0$	$X(\text{Fe})$	$X(\text{Ti})$	$X(\text{Sc})$	$X(\text{Ca})$	$X(\text{Si})$	$X(\text{O})$
DDC0	0.805	15.71	1.77(43)	0.91	-0.17	0.848	9699	1.527	8.46(-1)	1.18(-1)	1.58(-5)	5.58(-11)	2.52(-2)	4.00(-2)	2.76(-7)
DDC6	0.727	16.89	1.62(43)	0.98	-0.13	0.809	9297	1.422	7.24(-1)	1.15(-1)	2.14(-5)	8.63(-11)	4.00(-2)	8.95(-2)	6.83(-7)
DDC10	0.650	17.44	1.45(43)	1.01	-0.09	0.793	9129	1.342	6.13(-1)	1.08(-1)	2.38(-5)	1.10(-10)	4.89(-2)	1.36(-1)	1.12(-6)
DDC15	0.558	17.76	1.22(43)	1.03	-0.02	0.786	9019	1.263	4.54(-1)	9.27(-2)	2.43(-5)	1.48(-10)	5.60(-2)	2.14(-1)	2.05(-6)
DDC17	0.458	18.90	1.03(43)	1.10	0.05	0.738	8647	1.197	3.68(-1)	8.69(-2)	2.43(-5)	1.60(-10)	5.94(-2)	2.56(-1)	2.52(-6)
DDC20	0.344	19.38	7.65(42)	1.11	0.15	0.726	8504	1.091	1.95(-1)	6.70(-2)	2.02(-5)	2.10(-10)	5.65(-2)	3.62(-1)	4.46(-6)
DDC22	0.236	19.52	5.10(42)	1.09	0.65	0.721	8306	0.980	8.71(-2)	5.09(-2)	1.50(-5)	2.69(-10)	4.68(-2)	4.61(-1)	7.69(-6)
DDC25	0.180	20.50	3.64(42)	1.06	0.96	0.626	7338	0.920	3.49(-2)	4.06(-2)	9.58(-6)	3.44(-10)	3.29(-2)	5.51(-1)	2.18(-5)

Notes: Numbers in parentheses correspond to powers of ten. Q_{γ} is the ratio of the peak bolometric luminosity to the instantaneous rate of decay energy. The Lagrangian mass coordinate M_{τ} , velocity v_{τ} , temperature T_{τ} , and mass fractions X are given at the location where the inward-integrated electron-scattering optical depth $\tau_{\text{es}} = 2/3$. Note that the reported ^{56}Ni mass fraction corresponds to a time immediately after explosive burning ceases, rather than the time of bolometric maximum.

peak. It is only at nebular times that the SN radiation is directly tied to the instantaneous energy deposition rate. A fraction of the decay energy will inevitably escape the ejecta, even as early as maximum light. In our model series, the energy actually deposited in the ejecta is 85%–95% of the decay energy, resulting in a 4%–17% higher effective Q_{γ} (noted \tilde{Q} in Höflich & Khokhlov 1996).

We also obtain a fair agreement with the delayed-detonation model results of Höflich & Khokhlov (1996) for the peak bolometric luminosities, but our rise times are 3–8 d longer for a given ^{56}Ni mass and show a systematic increase for lower ^{56}Ni mass. The origin of the differences may be the opacity (and its associated impact on optical depth and the diffusion time), whose influence has been studied, e.g., by Khokhlov, Müller & Höflich (1993); Pinto & Eastman (2000a,b). Since the pre-peak phase is not the focus of this study, we defer a detailed discussion of this result, and comparisons to alternate works, to Blondin et al. (in prep).

At bolometric maximum, the “photospheric” radii¹ are on the order of $\sim 1.3\text{--}1.4 \times 10^{15}$ cm irrespective of the model, so that the range of luminosities reflects a modulation in temperature, from 9200 K in model DDC25 to 15270 K in model DDC0 at this location. Consequently, a trend of higher ejecta ionization is obtained for models with increased ^{56}Ni (Fig. 3). Combined with abundance variations in the spectrum formation region, these variations are at the origin of the basic diversity of SN Ia maximum-light spectra (Sect. 5).

With our sample of delayed-detonation models, which spans a range in ^{56}Ni mass from 0.18 to 0.81 M_{\odot} , we reproduce the full range of observed luminosities, B -band magnitudes and colours of SNe Ia at maximum light (Fig. 4). For example, our model set covers $B - R$ values from -0.17 to 0.96 mag at bolometric maximum (Table 2), and misses only a few of the brightest and bluest SNe Ia at peak (most of these are 91T-like). We also reproduce the small luminosity scatter in the near-infrared bands with respect to the optical (see Table C1), as first found observationally by Krisciunas, Phillips & Suntzeff (2004). The remarkable achievement of the delayed-detonation mechanism, which is not new, is that a single parameter can explain the most fundamental

¹ In SNe Ia, there is no clearly-defined photosphere due to the ubiquitous presence of lines and the sub-dominance of absorption/continuum processes. Hence, by this term, we broadly refer to the spectrum-formation region, and adopt for that region the location where the inward-integrated electron-scattering optical depth is $2/3$.

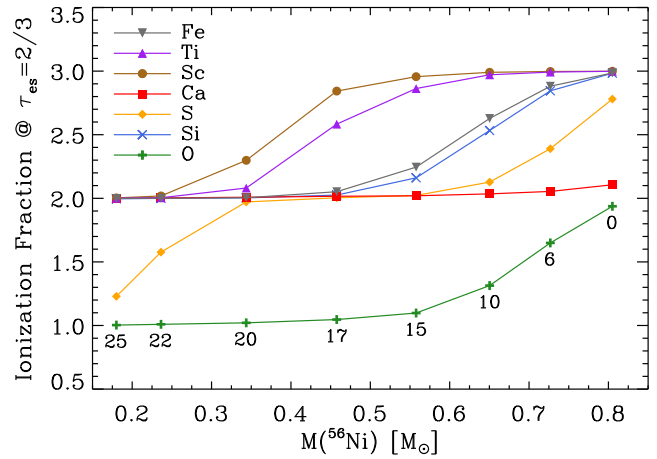


Figure 3. Ionization fraction at bolometric maximum for selected species as a function of ^{56}Ni mass, at the location where the inward-integrated electron scattering optical depth $\tau_{\text{es}} = 2/3$. We define the ionization fraction as $\sum_i iX^{i+} / \sum_i X^{i+}$, where X^{i+} is the mass fraction of ionization stage i for element X . Numbers below the curve for the oxygen ionization fraction correspond to the DDC model number.

properties of SN Ia light curves. In the next section, we show how well it reproduces the fundamental spectroscopic properties of a wide range of SNe Ia at bolometric maximum.

5 SPECTROSCOPIC PROPERTIES AT BOLOMETRIC MAXIMUM

5.1 Spectral Diversity, ionization sequence, and line blanketing

The spectral diversity of these delayed-detonation models, associated with variations in ejecta characteristics (temperature, ionization) and photometric properties (luminosity, colour) reflects closely the observed diversity of SNe Ia at maximum light (Fig. 5; see also Sect. 6). This is a real achievement given the much greater complexity of spectra compared to photometry (for example, a given model may reproduce the colour of a SN Ia but may match the spectrum poorly; see, e.g., Blondin et al. 2011). The theoretical spectral-energy distributions (SEDs) match satisfactorily the entire observed wavelength range from the blue, luminous, but spectro-

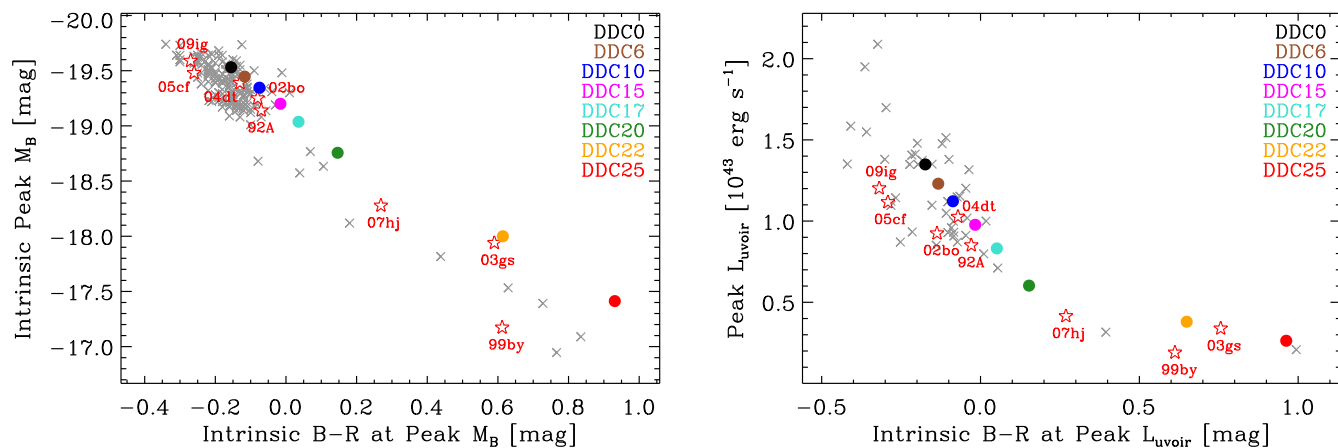


Figure 4. Intrinsic peak M_B (left) and UVOIR luminosity (right) vs. intrinsic $B - R$ colour at B -band and UVOIR maximum, respectively, for our sequence of delayed-detonation models. We overplot (grey crosses) the observed values using a wide sample of SNe Ia (similar to that used in Blondin et al. 2011). Star symbols correspond to objects that will be discussed individually and in greater detail in Sect. 6. Synthetic and observed UVOIR luminosities were derived from $UBVRI$ magnitudes (only $BVRI$ in the case of SN 2007hj) using the method of Valenti et al. (2008). We provide tabulated values of the bolometric luminosity and $UBVRIJHK$ magnitudes at bolometric maximum for our models in Table C1.

scopically normal SN 2009ig (model DDC0), to the redder, low-luminosity 91bg-like SN 1999by (model DDC25). For each intermediate model, we also find suitable matches. Models with a larger ^{56}Ni mass achieve a higher peak bolometric luminosity and bluer colours, which in spectra is best reflected with the stronger flux shortward of $\sim 4000 \text{ \AA}$. All these properties directly reflect the varying levels of temperature/ionization discussed in the preceding section.

With a total ^{56}Ni mass of $0.81 M_{\odot}$, model DDC0 matches the peak luminosity of several 91T-like SNe Ia but fails to reproduce their blue spectra characterized by lines of Fe III and very weak Si II 6355 \AA absorption. In the future, we will investigate if a delayed-detonation model with a (slightly) larger ^{56}Ni mass than DDC0 would yield a better agreement with 91T-like objects.

Irrespective of ^{56}Ni mass, our models are systematically faint in the UV. The total integrated flux blueward of 2500 \AA represents between $\sim 0.6\%$ (model DDC0) and $< 0.01\%$ (models DDC22 and DDC25) of the bolometric flux. This agrees with the few observations shown in Fig. 5, a subset of which have UV photometry obtained with the *Hubble Space Telescope* (SN 1992A, Kirshner et al. 1993; SN 2004dt, Wang et al. 2012) and the *Swift* satellite (SN 2005cf, Wang et al. 2009b; SN 2009ig, Foley et al. 2012). In addition, the inferred $uvw2 - v$ colours² range between ~ 2.5 mag (DDC0) and ~ 5 mag (DDC25), in line with those inferred by (Milne et al. 2010) using *Swift* observations of a large sample of SNe Ia.

The key spectroscopic signatures of SNe Ia are reproduced, such as the near-constant strength of the distinctive Si II 6355 \AA line in observations of low to high luminosity SNe Ia. In contrast, the relative depth at maximum absorption of the Si II 5972 \AA line is a strongly varying function of peak luminosity and colour (see Sect. 5.2). We also predict the presence at maximum light of the Ca II near-infrared triplet (8498, 8542, and 8662 \AA) and the emergence of a strong O I 7773 \AA line for SNe Ia with less than $\sim 0.4 M_{\odot}$ of ^{56}Ni . Both features are discussed in greater detail in Sections 5.3 and 5.4.

² The $uvw2$ and v filters have a central wavelength of 1941 \AA and 5441 \AA , respectively (Brown et al. 2010).

While the colour of the SED is in part set by the temperature/ionization of the spectrum formation region, another critical ingredient is line blanketing. At the peak of the light curve, the bulk of the radiation emerges from regions where the ejecta composition is dominated by IMEs and IGEs (see Table 2 and Fig. 1), whose associated line opacity supersedes the contributions from electron scattering and continuum processes. These different opacity sources may overlap but often do not, so that they effectively blanket the entire spectrum, leaving no gaps for radiation to escape except at much longer wavelengths. Hence, blanketing induces significant redistribution of the flux to longer wavelengths through absorption and fluorescence.

Figure 6 illustrates the impact of lines on the maximum-light spectra and suggests two types of influence. First, Si II, Ca II, Mg II, or O I produce few strong and isolated lines through transitions between low lying states, which affect a limited wavelength range, although for Ca II H&K, the width of the absorption can be as broad as the U -band filter (model DDC20; see Fig. B6)! Second and more dramatic is the presence of forests of lines from some species/ions, which effectively blanket the SN radiation. For example, S II causes significant blanketing in the 5500 \AA region (the effect is largest for models DDC15–DDC17) — the associated lines overlap and prevent the identification of any of them individually (although the strongest transitions produce the characteristic “W” feature; see Appendix B). Ionization also tunes the effects of Fe opacity, which is primarily due to Fe III at high ^{56}Ni mass and to Fe II for models less luminous at peak than DDC15.

More striking still is the sudden increase of Ti II and Sc II opacity in models with $\lesssim 0.4 M_{\odot}$ of ^{56}Ni (DDC20–DDC25), due to a shift to a lower ionization state (Fig. 3). This largely explains the progressive drop in the emergent flux blueward of $\sim 4500 \text{ \AA}$ in our synthetic spectra, which mirror the observations, as we progress in the model sequence from DDC0 to DDC25, i.e., from blue luminous SNe Ia to red low-luminosity 91bg-like SNe Ia. This effect may seem surprising given the low abundance of Ti and Sc in the ejecta (Table 1). The distribution of Ti is quite uniform throughout the ejecta with a mass fraction of $\sim 10^{-5}$ at $\tau_{\text{es}} = 2/3$ and beyond, such that the increasing impact of Ti II is entirely attributed to an ionization effect. In addition, abundance variations play a role for the Sc II lines, since the Sc mass fraction is $\sim 10^{-10}$ at $\tau_{\text{es}} = 2/3$

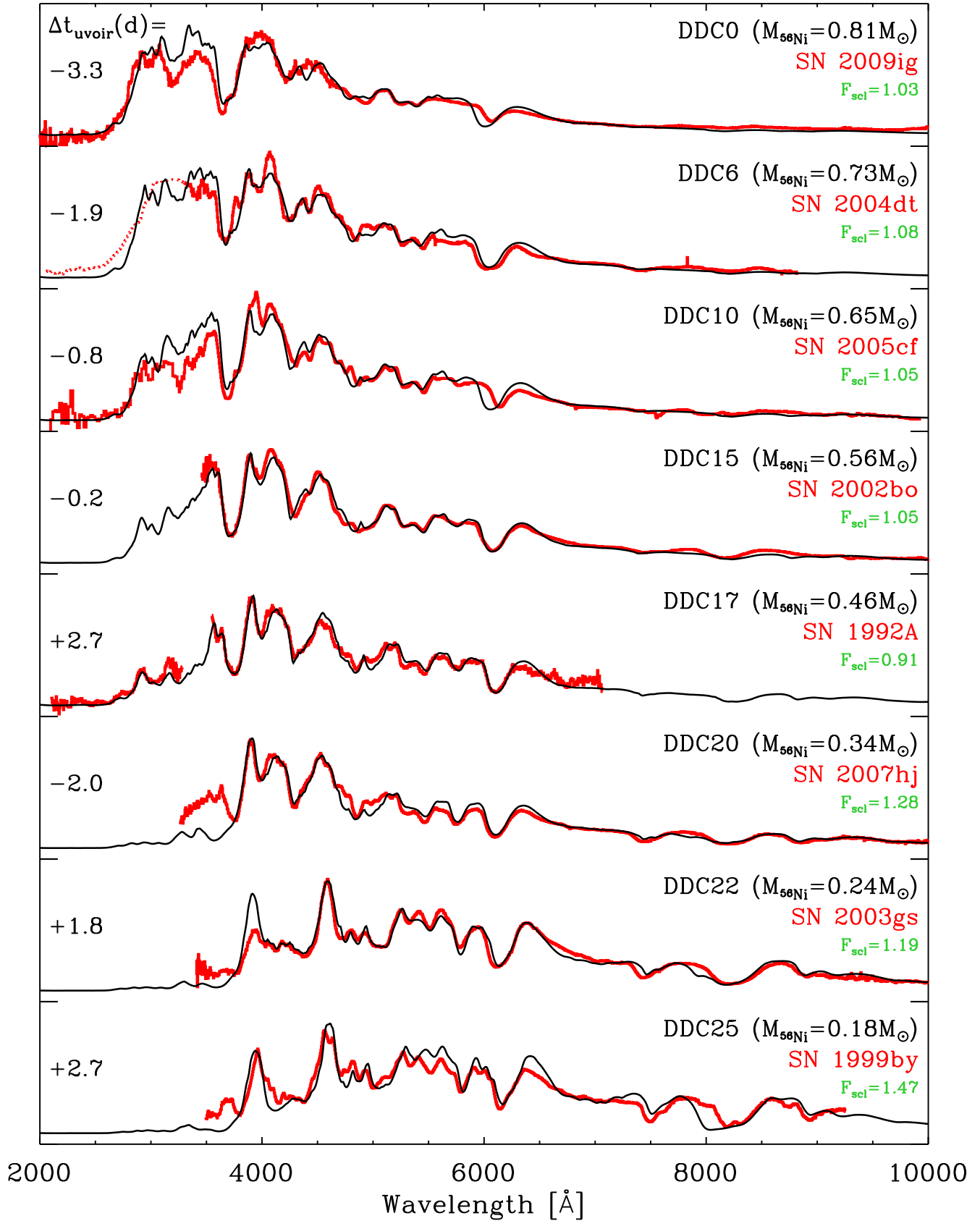


Figure 5. Comparison of synthetic spectra of delayed-detonation models (black) to observed SNe Ia near maximum light (red). The tickmarks on the ordinate give the zero-flux level. The time label corresponds to days from pseudo-bolometric (UVOIR) maximum. The observed spectra have been de-redshifted, de-reddened, and scaled to match the absolute V -band magnitude inferred from the corresponding SN Ia photometry. An additional scaling (F_{scI} ; green label) has been applied to the observed spectra to reproduce the mean synthetic flux in the range 4000–6000 Å. For SN 2004dt we add the low-resolution *HST* ACS grism spectrum (dotted line) published by Wang et al. (2012).

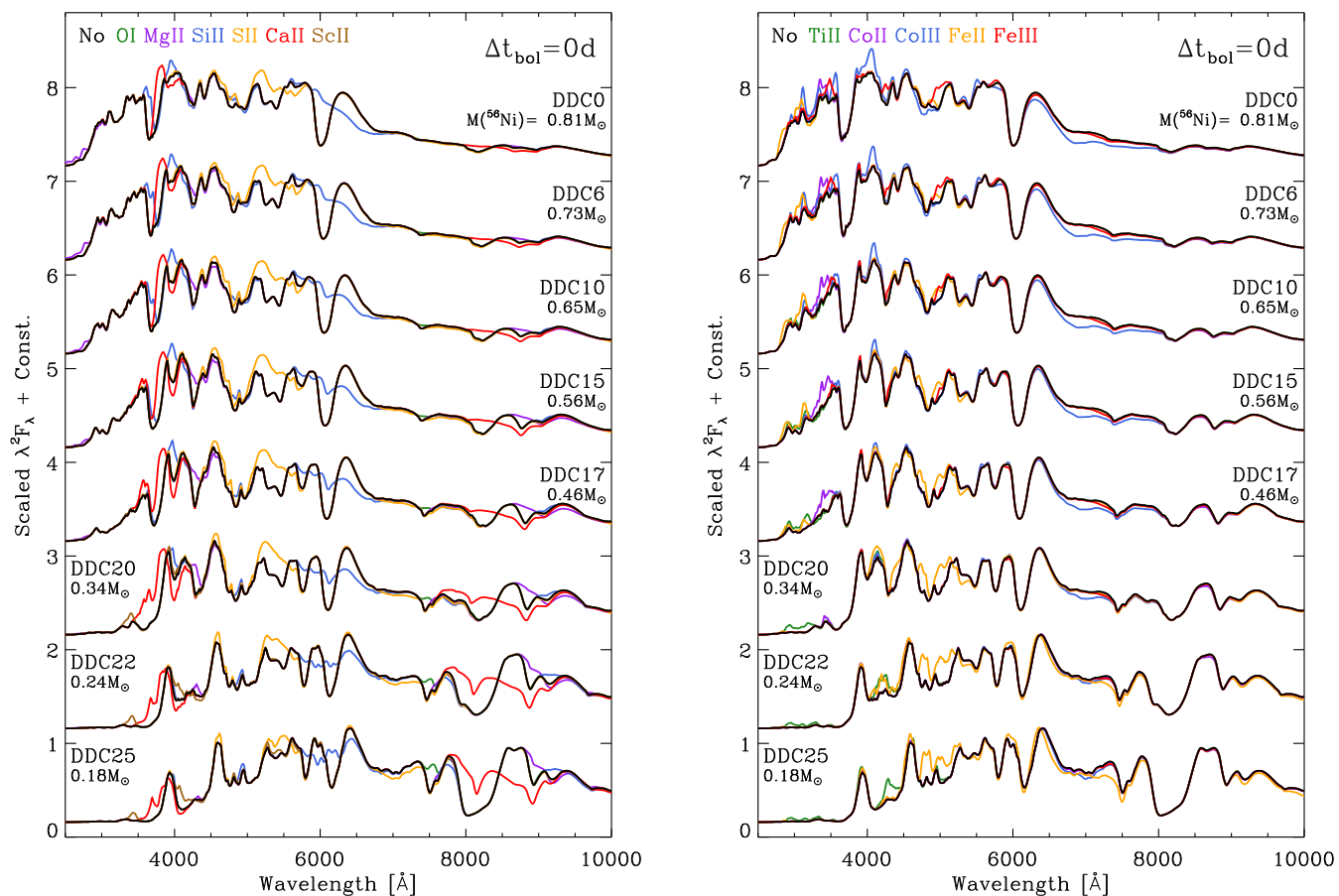


Figure 6. Comparison of synthetic spectra in our model series at bolometric maximum illustrating individual ion contributions to spectral features. Besides the total spectrum (black), the left panel shows the influence of O I, Mg II, Si II, S II, Ca II, and Sc II; the right panel shows that of Ti II, Co II, Co III, Fe II, and Fe III — the coloured lines correspond to synthetic spectra computed *ignoring* all bound-bound transitions of the corresponding ion. For better visibility of weak flux variations in the red, we show the quantity $\lambda^2 F_\lambda$.

(see Table 2), but reaches $\sim 10^{-5}$ at larger velocities. The influence of Ti II/Sc II opacity becomes particularly severe starting at model DDC22, which marks a transition to 91bg-like spectra, characterized by enhanced flux blocking over the range 4000–4500 Å. Note how this transition occurs over a very narrow range in ^{56}Ni mass (from 0.34 M_\odot for DDC20 to 0.24 M_\odot for DDC22), such that in principle a strict upper limit on the ^{56}Ni mass can be inferred from spectra with a 91bg-like morphology (in the context of a Chandrasekhar-mass delayed-detonation model).

5.2 The Si II 6355 Å line and the $\mathcal{R}(\text{Si})$ ratio

The defining spectroscopic feature of SNe Ia, namely the blueshifted Si II 6355 Å doublet absorption, remains broad (FWHM $\sim 12000 \text{ km s}^{-1}$) in models DDC0–DDC17 and only becomes noticeably narrower from DDC20 onwards, with FWHM $\sim 8000 \text{ km s}^{-1}$ in model DDC25, reflecting the stronger confinement of Si to the inner ejecta in models with a lower deflagration-to-detonation transition density (Fig. 1). The velocity at maximum absorption (v_{abs}) approximately reflects that of the peak Si abundance ($X_{\text{Si}} \sim 0.6$, regardless of the ^{56}Ni mass; see diamonds in Fig. 1), and varies smoothly between $\sim -17000 \text{ km s}^{-1}$ for DDC0 and $\sim -9000 \text{ km s}^{-1}$ for DDC25.

The relative depth at maximum absorption varies little amongst our model series, as the line is optically thick at this lo-

cation in all models (the Sobolev optical depth for the transition at 6347 Å varies between ~ 2 for DDC0 and ~ 387 for DDC25). This contrasts with the neighbouring Si II 5972 Å line which becomes progressively stronger with decreasing ^{56}Ni mass, transitioning from optically thin to thick ($\tau_{\text{Sob}}(5979 \text{ Å}) > 1$ at maximum absorption for models DDC20–25) and reflecting the drop in the Si ionization fraction (Fig. 3; see also Hachinger et al. 2008). The relative behaviour of both lines is a well-known spectroscopic characteristic of SNe Ia, and quantified in terms of the $\mathcal{R}(\text{Si})$ ratio (Nugent et al. 1995). In our models $\mathcal{R}(\text{Si})$ varies between $\lesssim 0.1$ (DDC0) and ~ 0.8 (DDC25), in good agreement with the observed variation (Fig. 7). Contrary to claims by Garnavich et al. (2004) we find no evidence for Ti II absorption in this wavelength region that could bias the $\mathcal{R}(\text{Si})$ ratio for low-luminosity SNe Ia (see Appendix B).

Branch et al. (2006) use the pseudo-equivalent widths (pEW) of the Si II 6355 Å and 5972 Å lines to classify SNe Ia into four subgroups, organized around the “Core Normal” subgroup which occupies a central position in this two-dimensional parameter space. SNe Ia with smaller and larger pEW(6355 Å) are termed “Shallow Silicon” (includes 91T-like SNe Ia) and “Broad Line”, respectively, while those with larger pEW(5972 Å) are dubbed “Cool” (includes 91bg-like SNe Ia), in reference to their lower ejecta temperatures. Our models belong to only two subclasses

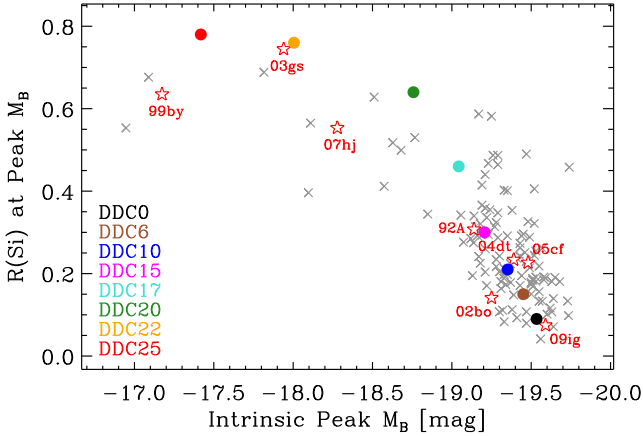


Figure 7. Spectroscopic ratio $\mathcal{R}(\text{Si})$ versus intrinsic peak M_B for our model set. We overplot (grey crosses) observed values from a large sample of SNe Ia (see Blondin et al. 2012). Star symbols correspond to objects that will be discussed individually and in greater detail in Sect. 6.

of this scheme, namely Broad Line (models DDC0–17) and Cool (DDC20–25) SNe Ia.

The classification scheme of Wang et al. (2009a) is based on the velocity at maximum absorption of the Si II 6355 Å feature, and divides SNe Ia into Normal and High-velocity subclasses. SNe Ia with 91T-like or 91bg-like spectra (including SNe Ia with $\mathcal{R}(\text{Si}) > 0.5$) are not classified according to this scheme. As noted in Sect. 5.1 there are no 91T-like spectra in our model series, while models DDC20–25 either have $\mathcal{R}(\text{Si}) > 0.5$ (DDC20) or display 91bg-like spectra (DDC22–25). The remaining models (DDC0–17) would all be part of the High-velocity subclass (i.e., $v_{\text{abs}} \lesssim -12000 \text{ km s}^{-1}$; see, e.g., Blondin et al. 2012).

There are thus no Core Normal (Branch et al. 2006) or Normal (Wang et al. 2009a) SNe Ia amongst our model set. The Si II 6355 Å line in our synthetic spectra is systematically broader and more blueshifted than observed in these two subclasses, suggesting the ejecta kinetic energy in our models is too large to account for the bulk of SNe Ia³. However, the impact is often only visible in the Si II lines (4130 Å, 5972 Å, and 6355 Å), while other spectroscopic features are well matched (e.g., Ca II H&K and the S II “W” feature in the comparison between model DDC10 and SN 2005cf in Fig. 5), such that some of our models closely resemble Core Normal SNe Ia despite the Si II 6355 Å mismatch (DDC0 and DDC10). If this were solely a problem related to the ejecta kinetic energy then *all* lines should be too broad. Our limitation to 1D also overlooks potential viewing-angle effects in an aspherical ejecta, which can significantly impact the width and blueshift of the Si II 6355 Å line, as shown by Blondin et al. (2011) based on the 2D delayed-detonation models of Kasen, Röpke & Woosley (2009).

5.3 The O I 7773 Å line as an abundance tracer

The evolution in strength and morphology of the O I 7773 Å line profile in our synthetic spectra reproduces well the observed sequence. This line becomes progressively stronger with decreasing

³ The simplified reduced nuclear kinetics scheme used in our models (see Sect. 2.1) may lead to an overestimation of the asymptotic kinetic energy. Hydrodynamical simulations with detailed nuclear kinetics are planned to quantify the difference.

⁵⁶Ni mass along our model sequence (Fig. 6, left; green line). It is essentially non-existent in models DDC0–10, barely noticeable in models DDC15 and DDC17, only to strongly imprint the spectra from model DDC20 onwards. This evolution follows the gradual decrease in the ionization fraction for O from ~ 2.0 to 1.0 (Fig. 3), but seems primarily influenced by the varying oxygen abundance with ⁵⁶Ni mass (factor ~ 5 variation in total oxygen mass between DDC0 and DDC25) and the resulting chemical stratification in velocity. The velocity at which $X(\text{O}) = 10^{-3}$ drops from $\sim 17500 \text{ km s}^{-1}$ in model DDC0 to $\sim 9200 \text{ km s}^{-1}$ in model DDC25, while the corresponding “photospheric” velocities are 9699 and 7338 km s^{-1} , respectively (Table 2). We thus associate this behavior of the O I line with an abundance effect resulting from the ejecta stratification in velocity.

The O I 7773 Å line can in principle be used as a probe of left-over unburnt oxygen. However, unlike C II lines which provide an unambiguous signature of unburnt carbon, the only definite signature of unburnt oxygen (as opposed to O produced via carbon burning) in our models is through the detection of absorption out to velocities where we recover the initial $X(\text{O}) \approx 0.5$ composition. The minimum velocity at which $X(\text{O}) \approx 0.5$ varies between $\sim 20000 \text{ km s}^{-1}$ (model DDC25) and $\sim 35000 \text{ km s}^{-1}$ (model DDC0), and we obtain no O I 7773 Å absorption out to these velocities in any of our models. This is likely a shortcoming of spherical symmetry, as multi-D effects are considered essential to preserve O (and C) unburnt in the ejecta, even at the relatively low velocities corresponding to the spectral-formation region at bolometric maximum (see Gamezo, Khokhlov & Oran 2005).

5.4 Impact of Ca II lines and high-velocity features

The large drop in flux around $\sim 3500 \text{ Å}$ between model DDC17 and DDC20 is mainly due to an opacity increase associated with Ca II. While the Ca ionization fraction at $\tau_{\text{es}} = 2/3$ stays fairly constant from models DDC0 to DDC25, it changes significantly at velocities $\gtrsim 15000 \text{ km s}^{-1}$ (Fig. 8). Since the Ca II H&K lines remain optically thick out to large velocities, absorbing well beyond 30000 km s^{-1} in all models, such ionization changes have a noticeable impact on the emergent flux in the *U* band.

The effect is more clearly visible in the Ca II near-infrared triplet, which remains weak in all models up to DDC17 and becomes progressively stronger up to DDC25, with a line-profile morphology displaying high-velocity components (see inset in Fig. 8). Such high-velocity features (HVFs) were associated with density or abundance enhancements by Mazzali et al. (2005), possibly resulting from multi-dimensional effects in the explosion itself or from interaction with circumstellar material. Our simulations suggest that HVFs in Ca II can even arise in spherically symmetric ejecta, primarily through optical-depth effects due to ionization changes occurring at large velocity. Abundance effects play no role here: the Ca mass fraction at 15000 km s^{-1} is three orders of magnitude lower in model DDC25 ($\sim 4.1 \times 10^{-5}$), which displays prominent HVFs, compared to model DDC0 ($\sim 3.4 \times 10^{-2}$), which displays a single weak absorption. Furthermore, there is no density bump at these velocities. Obviously, when such HVFs are associated with a variation in the polarization signal across the line (e.g., in SN 2001el; Wang et al. 2003), a departure from spherical symmetry must occur, but these two signatures (HVF and polarization) can arise independently of one another.

In all of our models with more than $0.4 M_{\odot}$ of ⁵⁶Ni (DDC0–17), the Ca II H&K absorption feature is strongly contaminated by the Si II 3858 Å doublet, resulting in double-absorption features

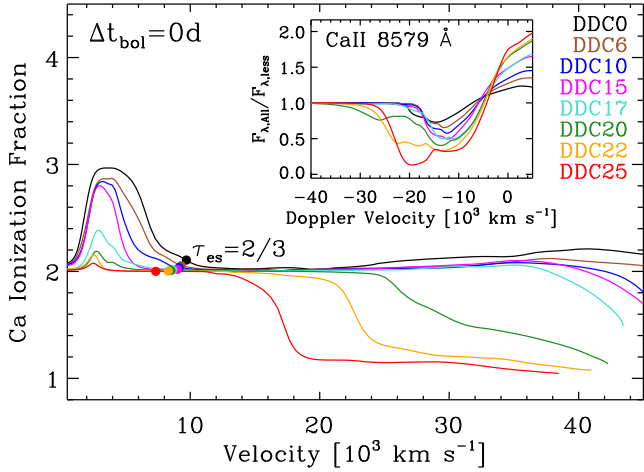


Figure 8. Ionization fraction for Ca at bolometric maximum as a function of velocity. The solid dots indicate the location where the inward-integrated electron scattering optical depth $\tau_{\text{es}} = 2/3$. The inset shows Ca II near-IR triplet line profiles computed as the ratio of the full spectrum ($F_{\lambda, \text{All}}$) to that excluding all Ca II bound-bound transitions ($F_{\lambda, \text{less}}$), revealing high-velocity absorption features in models with less ^{56}Ni .

(see Appendix B). These are occasionally mistaken for “photospheric” and “high-velocity” components of Ca II H&K (see discussion in Lentz et al. 2000).

6 INDIVIDUAL COMPARISONS OF DELAYED-DETONATION MODELS TO OBSERVATIONS AT MAXIMUM LIGHT

For each Chandrasekhar-mass delayed-detonation model in our set we are able to find a good match to an observed SN Ia (Fig. 5). In most cases there are several observed SNe Ia that match a given model — this is not surprising given the overall spectral homogeneity of SNe Ia with a given luminosity (see, e.g., Blondin et al. 2012). In those cases we preferentially select SNe Ia whose spectra cover the largest wavelength range (i.e. extending blueward of Ca II H&K and redward of the Ca II NIR triplet). The comparison between synthetic and observed spectra is largely based on a “chi-by-eye” estimate of the overall SED match, with particular emphasis on the flux level in the *U* and *B* bands, as well as individual spectroscopic features. This approach is fine to assess the broad compatibility of delayed-detonation models — given the recognized influence of multi-D effects and our 1D approach, a perfect match may be coincidental. We use the Supernova Identification (SNID) code of Blondin & Tonry (2007) to ease our exploration of the largest possible data set, but make no attempt at quantifying the strength of the correlation between synthetic and observed spectra as done by Blondin et al. (2011).

6.1 DDC0 ($M_{56\text{Ni}} = 0.81 M_{\odot}$) vs. SN 2009ig

The spectra of SN 2009ig (Foley et al. 2012) are well reproduced by DDC0 over the wavelength range 2000–10000 Å. We use the same distance modulus as Foley et al. (2012) (from Tully & Fisher 1988), but a larger extinction ($A_V = 0.3$ mag from our own fits to the light curves using the BayeSN statistical model of Mandel, Narayan & Kirshner 2011). Foley et al. (2012) do note however the presence of significant interstellar Na I absorption

($EW = 0.4$ Å) at the redshift of the host galaxy, consistent with visual extinctions in the range $0 \lesssim A_V \lesssim 1$ mag (see Blondin et al. 2009, their Fig. 5).

SN 2009ig is a “Core Normal” SN Ia according to the Branch et al. (2006) classification scheme (Blondin et al. 2012). We are thus unable to reproduce its narrow Si II 6355 Å line profile (see Sect. 5.2). There is only a minor mismatch, however, in the width of other features, such as the Ca II H&K absorption (contaminated by Si II 3858 Å in the blue; see Sect. 5.4 and Fig. B1). The comparison at -3.3 d is impressive overall, although it is not as good for spectra closer to maximum light, in particular in the region 3000–3500 Å where the model is brighter than observations. The ratio of peak UVOIR luminosities is comparable ($Q_{\text{UVOIR}} = 1.12$) to the scaling to match the mean fluxes in the 4000–6000 Å region ($F_{\text{sc1}} = 1.03$), confirming the good correspondence between the model and the data.

The peak luminosity and colours of DDC0 match well the luminous SN 1999ac (Garavini et al. 2005; Phillips et al. 2006) and SN 2001eh (Sauer et al. 2008), although our synthetic line profiles are systematically too broad (in particular Ca II H&K, in addition to Si II 6355 Å) with respect to the observations.

Model DDC0 also reproduces the overall SED and spectroscopic features of the luminous yet spectroscopically normal SN 1999ee (Hamuy et al. 2002), and matches well its peak luminosity ($Q_{\text{UVOIR}} = 0.98$), although the flux level blueward of ~ 3500 Å is too high in our synthetic spectrum.

6.2 DDC6 ($M_{56\text{Ni}} = 0.73 M_{\odot}$) vs. SN 2004dt

SN 2004dt has some interesting properties. Its Si II 6355 Å line displays prominent HVFs up until a few days past maximum light, which led Altavilla et al. (2007) to invoke an enhanced density structure in the outer layers. Furthermore, it displays a UV excess around maximum light compared to other SNe Ia, which led Wang et al. (2012) to invoke viewing-angle effects associated with large-scale ejecta asymmetries. Interestingly, our smooth 1D model DDC6 reproduces the line widths, the overall SED, and the strong UV flux of SN 2004dt. (The dotted line in Fig. 5 shows an *HST* UV grism spectra taken with the ACS instrument — the resolution is very low so we are not concerned with small-scale absorption features.)

We find an excellent match to the peak luminosity, colours, and early-time spectra of SN 2006cp (Blondin et al. 2012), although the published spectra span a limited wavelength range (3500–7500 Å) and none are within 5 d from *B*-band maximum light.

6.3 DDC10 ($M_{56\text{Ni}} = 0.65 M_{\odot}$) vs. SN 2005cf

SN 2005cf is a “golden standard” amongst SNe Ia according to Wang et al. (2009b). The match of the maximum-light spectra to model DDC10 is excellent overall in the range 2000–10000 Å, although the Si II lines (4130 Å, 5972 Å, and 6355 Å) are significantly narrower and less blueshifted than in our synthetic spectrum (as expected since this SN is part of the Core Normal subclass; see Sect. 5.2). The widths of other features, such as Ca II H&K and the S II “W”, are nonetheless compatible with our model. The Ca II H&K absorption displays a double-absorption profile whose blue component is mostly due to contamination by Si II 3858 Å (Sect. 5.4 and Fig. B3). Model DDC10 also reproduces the UV flux for this SN, measured using the *Swift* satellite, and matches perfectly the observed UVOIR flux ($Q_{\text{UVOIR}} = 1.00$).

Table 3. Comparison of delayed-detonation models to observed SNe Ia near maximum light.

Model	$M(^{56}\text{Ni})$ [M_{\odot}]	t_{rise} [day]	L_{bol} [erg s^{-1}]	L_{uvoir} [erg s^{-1}]	SN	Ref.	μ [mag]	Method	$E(B - V)$ [mag]	Q_{uvoir}	Δt_{uvoir} [day]	F_{scl}
(1)	(2)	(3)	(4)	(5)	(6)	(7)	(8)	(9)	(10)	(11)	(12)	(13)
DDC0	0.805	15.71	1.77(43)	1.20(43)	2009ig	1	32.60	TF	0.14	1.12	-3.3	1.03
DDC6	0.727	16.89	1.62(43)	1.03(43)	2004dt	2,3	34.44	z_{CMB}	0.04	1.20	-1.9	1.08
DDC10	0.650	17.44	1.45(43)	1.12(43)	2005cf	4,5	32.17	SN Ia	0.22	1.00	-0.8	1.05
DDC15	0.558	17.76	1.22(43)	9.25(42)	2002bo	6	31.90	SN Ia	0.41	1.06	-0.2	1.05
DDC17	0.458	18.90	1.03(43)	8.51(42)	1992A	7	31.63	SBF	0.02	0.98	+2.7	0.91
DDC20	0.344	19.38	7.65(42)	4.15(42)	2007hj	8	33.88	z_{Virgo}	0.11	1.32	-2.0	1.28
DDC22	0.236	19.52	5.10(42)	3.39(42)	2003gs	9	31.65	SBF	0.07	1.12	+1.8	1.19
DDC25	0.180	20.50	3.64(42)	1.91(42)	1999by	10	30.74	Cepheids	0.03	1.38	+2.7	1.47

Notes: Numbers in parentheses correspond to powers of ten. **Column information:** (1) Model name; (2) mass of synthesized ^{56}Ni ; (3) rise time to peak bolometric luminosity. Note that the rise to UVOIR maximum is ~ 0.5 –1 d longer than to the true bolometric maximum; (4) peak bolometric luminosity; (5) peak UVOIR luminosity derived from synthetic *UBVRI* magnitudes using the method of Valenti et al. 2008; (6) name of observed SN Ia used for comparison in Fig. 5; (7) reference for spectroscopic data used in Fig. 5 (see References below); (8) distance modulus (assuming $H_0 = 73 \text{ km s}^{-1} \text{ Mpc}^{-1}$ where applicable); (9) method for distance modulus determination: SBF=Surface Brightness Fluctuations, SN Ia=SN-based distance, TF=Tully Fisher, z_{CMB} =CMB-frame redshift-based distance modulus; z_{Virgo} =distance modulus based on the recession velocity corrected for the influence of the Virgo cluster; (10) total (Galactic and host-galaxy) reddening. Galactic reddening values are based on the infrared dust maps of Schlegel, Finkbeiner & Davis (1998), while host-galaxy reddening was inferred based on our own fits to optical (and NIR when available) SN lightcurves. For SN 2003gs we use the reddening reported by Krisciunas et al. (2009); (11) ratio of synthetic to observed peak UVOIR luminosities, derived from *UBVRI* magnitudes (only *BVRI* in the case of SN 2007hj) using the method of Valenti et al. 2008; (12) phase of SN with respect to the time of UVOIR maximum; (13) scale factor applied to the observed spectra to match the mean synthetic flux in the wavelength range 4000–6000 Å.

References: (1): Foley et al. 2012, (2): Altavilla et al. 2007, (3): Wang et al. 2012, (4): Garavini et al. 2007, (5): Bufano et al. 2009, (6): Benetti et al. 2004, (7): Kirshner et al. 1993, (8): Silverman et al. 2012, (9): Kotak et al. (in prep.), (10): Garnavich et al. 2004

The broader Si II lines in the spectra of SN 1997bp (Blondin et al. 2012) are better matched by DDC10, but this SN only has published spectra in the range 3500–7500 Å.

6.4 DDC15 ($M_{56\text{Ni}} = 0.56 M_{\odot}$) vs. SN 2002bo

There are only SN-based distances to SN 2002bo, which vary by ~ 0.5 mag in distance modulus (i.e. $\sim 20\%$ in absolute distance). This uncertainty stems in part from the large reddening inferred for this SN ($E(B - V) \approx 0.4$ mag, the largest of our comparison sample; see Table 3). We adopt the distance modulus of 31.90 mag inferred from NIR light curves (Wood-Vasey et al. 2008), less subject to extinction than the visual bands. A similar distance modulus is derived from NIR light curves of the highly-reddened SN 2002cv ($\mu = 31.85$ mag assuming $H_0 = 73 \text{ km s}^{-1} \text{ Mpc}^{-1}$; Wood-Vasey et al. 2008), which occurred in the same host galaxy as SN 2002bo. Our inferred host-galaxy reddening ($E(B - V) = 0.39$ mag from our own fits to the lightcurves using the BayeSN statistical model of Mandel, Narayan & Kirshner 2011) is consistent with published estimates (e.g., Benetti et al. 2004). The authors of this latter paper argue based on spectroscopic modelling that a lower value of the reddening ($E(B - V) \approx 0.30$ mag) is needed to match the maximum-light spectrum, although their synthetic spectra systematically overestimate the flux redward of ~ 6500 Å due to their assumption of an inner diffusive boundary (their Fig. 17).

The synthetic spectrum of model DDC15 and the observations of SN 2002bo nearly overlap. The peak UVOIR luminosity is well reproduced ($Q_{\text{uvoir}} = 1.06$, i.e. better than 10%), as are the magnitudes at bolometric maximum in the optical and NIR bands (see Table C1).

We obtain equally-good matches to SN 2002dj (Pignata et al. 2008), SN 2004fu, and SN 2007co (both with spectra published by Blondin et al. 2012), all of which are also Broad Line SNe Ia of comparable luminosity.

A decent match is also found to the nearby SN 2011fe (Nugent et al. 2011), although our model DDC15 is significantly redder at maximum light (but of comparable luminosity, with $Q_{\text{uvoir}} \approx 1.1$). Röpke et al. (2012) found a reasonable match to SN 2011fe using a 3D delayed-detonation model tuned to synthesize $0.6 M_{\odot}$ of ^{56}Ni , although they argue that the agreement at maximum light is better for their violent WD merger model.

DDC15 is also a good match to SN 2001ay, for which Baron et al. (2012) invoke a pulsating delayed detonation model with a special WD configuration (excess C abundance and low central density). Our standard delayed-detonation model DDC15 is able to reproduce the peak UVOIR luminosity ($Q_{\text{uvoir}} = 1.05$) and colours, as well as the broad spectroscopic features (in particular Si II 6355 Å).

6.5 DDC17 ($M_{56\text{Ni}} = 0.46 M_{\odot}$) vs. SN 1992A

Kirshner et al. (1993) present an extensive set of UV spectra for SN 1992A taken with the International Ultraviolet Explorer (*IUE*) as well as *HST*. The maximum-light spectrum shown in Fig. 5 is a combination of an *IUE* UV spectrum and a CTIO optical spectrum. Kirshner et al. (1993) obtain reasonable fits to the observed spectra using a parameterized steady-state LTE radiative transfer calculation of the delayed-detonation model DD4 of Woosley (1991). Our full non-LTE time-dependent calculation reproduces the spectrum over the entire observed wavelength range, and is consistent with the inferred peak UVOIR luminosity ($Q_{\text{uvoir}} = 0.98$).

SN 2004eo (labeled “transitional” by Pastorello et al. 2007) is also a fair match to model DDC17, although $Q_{\text{uvoir}} \approx 0.7$, i.e. model DDC17 is fainter. Yet its ^{56}Ni mass ($0.46 M_{\odot}$) is $\sim 0.1 M_{\odot}$ larger than that inferred by Mazzali et al. (2008) based on modelling a single nebular-epoch spectrum ($0.38 M_{\odot}$). However, Mazzali et al. (2008) note that their inferred ^{56}Ni mass falls short of reproducing the peak bolometric luminosity, and revise their es-

timate to $0.43 \pm 0.05 M_{\odot}$, in agreement with model DDC17. A clear asset of our approach is the simultaneous calculation of the light curves and the spectra, which ensures the overall spectral morphology accurately reflects the SN luminosity.

6.6 DDC20 ($M_{56\text{Ni}} = 0.34 M_{\odot}$) vs. SN 2007hj

Model DDC20 corresponds to a transition from standard to low-luminosity SNe Ia, with the noticeable impact of increasing blanketing from Ti II/Sc II around $\sim 4000 \text{ \AA}$.

A good match is found to SN 2007hj. This SN is slightly bluer than the model but the relative strengths of spectral features is well reproduced, in particular the 4000–4500 \AA range, the S II “W” feature, the Si II lines (5972 \AA and 6355 \AA) and corresponding $\mathcal{R}(\text{Si})$ ratio, the O I 7773 \AA absorption, the Ca II near-IR triplet, as well as the Mg II feature at $\sim 8800 \text{ \AA}$ (see Fig. B6). There are however significant differences in the blue wing of the Ca II H&K line which is strongly suppressed in the model mainly due to Ca II absorption out to high velocities (see Sect. 5.4). Lines of Ti II and Sc II also deplete the flux in this region.

The spectroscopic features of SN 1998bp (Matheson et al. 2008) and SN 2007au (Blondin et al. 2012) are well matched by model DDC20, but the predicted luminosity is too high ($Q_{\text{uvoir}} = 1.91$ and 1.62 , respectively). The match to SN 2000dk (Matheson et al. 2008) is of comparable quality as the match to SN 2007hj, although the discrepancy in the blue wing of Ca II H&K is even larger (the luminosity is however in better agreement, with $Q_{\text{uvoir}} = 0.85$).

6.7 DDC22 ($M_{56\text{Ni}} = 0.24 M_{\odot}$) vs. SN 2003gs

With DDC22 we enter the category of subluminous SNe Ia, with the characteristic broad Ti II/Sc II absorption feature over the range 4000–4500 \AA .

An impressive match is found for SN 2003gs, a low-luminosity SN Ia in the optical bands (though slightly more luminous than 91bg-like SNe Ia). We assume the time of UVOIR maximum to coincide with the first photometric measurement (which in turn corresponds to the inferred time of V -band maximum by Krisciunas et al. 2009) since there are no pre-maximum observations for this SN. We expect the impact on the derived ratio of peak UVOIR luminosities ($Q_{\text{uvoir}} = 1.12$) to be minor, given the coincidence within 1 d of the times of UVOIR and V -band maxima in model DDC22. We checked that using the corrected U -band photometry recently published by Krisciunas et al. (2012) had no noticeable impact on the derived Q_{uvoir} .

While the flux in the blue wing of Ca II H&K compares better than for model DDC20 versus SN 2007hj, the predicted HVFs in the Ca II near-IR triplet are not present in the observations.

The spectroscopic features of SN 1998de (Matheson et al. 2008) are well matched by model DDC22, but the predicted luminosity is much too high ($Q_{\text{uvoir}} = 2.5$ based on $BVRI$ photometry only).

6.8 DDC25 ($M_{56\text{Ni}} = 0.18 M_{\odot}$) vs. SN 1999by

Model DDC25 corresponds to the classical low-luminosity 91bg-like SNe Ia. The overall SED and individual spectral features match up nicely with the well-observed 91bg-like SN 1999by (Garnavich et al. 2004). We encounter the same problem as in model DDC22 concerning the prediction of prominent HVFs in

the Ca II near-IR triplet. The model appears slightly over-luminous with respect to this SN ($Q_{\text{uvoir}} = 1.38$), but using only a 1σ larger Cepheid distance to the host galaxy NGC 2841 (i.e. $\mu = 30.97$ mag instead of $\mu = 30.74$ mag; Macri et al. 2001) results in a better agreement, with $Q_{\text{uvoir}} \approx 1.1$ (i.e. 10% shift in absolute flux). This model compares well to other 91bg-like SNe Ia, such as the eponymous SN 1991bg (Filippenko et al. 1992; Leibundgut et al. 1993) and SN 2005bl (Taubenberger et al. 2008).

We thus confirm the result of Höflich et al. (2002), that low-luminosity SNe Ia can be explained within the framework of Chandrasekhar-mass delayed-detonation models, contrary to claims otherwise (e.g., Pakmor et al. 2011). We will need, however, to see how our delayed-detonation models fare at pre-maximum phases through to the nebular phase.

Howell et al. (2001) show evidence for a significant intrinsic polarization level of ~ 0.3 – 0.8% in SN 1999by near maximum light, and argue that this SN has a well-defined symmetry axis, possibly resulting from a rapidly-rotating single WD or a binary WD merger process. Our excellent fits to the observed spectra with a 1D radiative transfer code suggest that such asymmetries, if present, do not dramatically affect the observables around peak bolometric luminosity.

7 DISCUSSION AND CONCLUSION

In this paper, we have presented a first effort at modeling SNe Ia with CMFGEN. Our 1D approach solves the radiative-transfer problem for SN Ia ejecta with a high level of physical consistency, which comes at a great computational expense. The coupled set of time-dependent statistical equilibrium, gas energy, and radiative transfer (0^{th} and 1^{st} moments) equations are solved for simultaneously, yielding multi-epoch SN Ia spectra from the UV to the infrared. The bolometric luminosity and the photometry are obtained by suitable integrations of that wavelength-dependent flux. Importantly, line blanketing is treated explicitly and consistently — the algorithm makes no assumption about the thermalization character of the opacity as typically done in approaches that do not solve for the level populations directly.

We compute radiative properties for a sequence of delayed-detonation models (Khokhlov 1991), a mechanism in which a deflagration is followed, after some delay depending on some prescribed transition density, by a detonation in a Chandrasekhar-mass white dwarf. This model is not new, and our investigation comes after nearly two decades of study of this mechanism (Khokhlov 1991; Khokhlov, Müller & Höflich 1993; Höflich, Khokhlov & Wheeler 1995; Höflich & Khokhlov 1996; Höflich et al. 2002; Gamezo, Khokhlov & Oran 2005). However, we present results that have a higher level of physical consistency than previously achieved, albeit in 1D.

Our models start at 1 d after explosion and are evolved with CMFGEN until beyond the bolometric peak. In this paper, we focus on the phase of bolometric maximum of such delayed-detonation models. We analyze their properties and compare them with publicly-available SN Ia data. For each model in the delayed-detonation sequence, best characterized by a ^{56}Ni mass ranging from 0.18 to $0.81 M_{\odot}$, we generally find a SN Ia that fits the peak bolometric flux to within $\sim 10\%$, and the colors to within ~ 0.1 mag. The spectral features are typically reproduced with high fidelity, both in strength and width.

Remarkably, with our set of delayed-detonation models, we reproduce the basic morphological diversity of SN Ia radia-

tive properties, from blue, luminous, yet spectroscopically-normal SNe Ia (e.g., SN 2009ig), to low-luminosity 91bg-like SNe Ia (e.g., SN 1999by). Our assessment is based primarily on optical data where the bulk of the SN Ia flux emerges, but we include UV data from the *Hubble Space Telescope* and the *Swift* satellite when available. We find that the rise time to bolometric maximum increases from ~ 15 to ~ 21 d with decreasing ^{56}Ni mass. Despite the complexity of our calculations, and the simplicity of Arnett’s rule (Arnett 1979, 1982), we support its validity to within 10% in such delayed-detonation models. Hence, at its maximum, the bolometric luminosity of SNe Ia is close to the instantaneous rate of decay energy, although both quantities are directly related only at nebular phases (and physically equivalent in the case of full γ -ray trapping).

We infer that the spectra of SNe Ia at maximum light primarily reflect the change in ionization balance resulting from the magnitude (and to a lesser extent, distribution) of heating from ^{56}Ni decay. A reduction in temperature causes a reduction of the flux in the blue, which is further exacerbated by a growing opacity from recombining ions like Ti, Sc, or Fe. This effect is particularly severe in the *U* and *B* bands for models with a ^{56}Ni mass less than $\sim 0.3 M_{\odot}$, and causes the transition to 91bg-like SN Ia spectra.

Reproducing the line widths is more prone to error due to our 1D approach, and the large ejecta kinetic energy in the explosion models, which leads to broader lines than observed in the bulk of SNe Ia. This problem seems however to affect mainly the Si II lines, while others (e.g., Ca II H&K, which overlap with Si II 3858 Å in the blue, and the S II “W” feature around 5500 Å) match the observations. Across our model set, we reproduce satisfactorily the widths of most features, the near-constant strength of Si II 6355 Å, and the strong dependence of $\mathcal{R}(\text{Si})$ on ^{56}Ni mass.

Ionization effects are particularly important for Ca II lines. In weaker explosions, Si II 6355 Å appears narrower when the Ca II near-IR triplet lines follow the opposite trend and appear broader and stronger. While the former represents an interesting diagnostic of the explosion energy, the latter is more sensitive to ionization. In the delayed-detonation model with the least amount of ^{56}Ni , ionization kinks give rise to high-velocity features in Ca II near-IR triplet: such “structures” are spherical shells of distinct Ca ionization, producing optical-depth variations that affect line profiles although they would produce no polarization signature.

In our model ejecta, there is essentially no carbon left by the detonation, even if it is weak. This is not a shortcoming of the delayed-detonation mechanism, but rather a problem with the assumption of spherical symmetry for the explosion phase (Gamezo, Khokhlov & Oran 2005). So, while ionization is key, abundances can also completely inhibit the formation of certain lines. The O 17773 Å line is in principle a useful probe of unburnt oxygen, although none of our maximum-light spectra shows O I absorption out to velocities where we recover the initial $X(\text{O}) \approx 0.5$ composition of the progenitor WD. Nonetheless, our models reproduce the observed trend of increasing O 17773 Å absorption with decreasing luminosity at maximum light, and we obtain no O signature in our (1D) delayed-detonation models that have a ^{56}Ni mass $\gtrsim 0.4 M_{\odot}$.

Even today, the inferences on the WD ejecta mass are not sufficiently accurate to establish whether it is the Chandrasekhar mass, or more, or less. At present, both M_{Ch} and sub- M_{Ch} models are compatible with observations (Höflich & Khokhlov 1996; Sim et al. 2010). Hence, an answer to this most fundamental question is still lacking. To identify a good model for a SN Ia, fitting the light curve is mandatory but it is clearly not sufficient. Fitting

the spectra is critical, and doing so simultaneously, with the same physics, is an asset. However, one must ensure a suitable match to observations at all times, not just at maximum light as done in this paper. In particular, explosion models are expected to best reveal their differences shortly after explosion (e.g. through presence or absence of unburnt material) or at nebular times when the IGE core (and possibly the innermost ^{56}Ni -deficient region) is revealed.

Moreover, one is faced with the role of multi-D effects, which may alter the spectral appearance sizeably for different viewing angles (Kasen, Röpke & Woosley 2009). As we demonstrate here, assuming spherical symmetry may still be suitable at certain epochs (e.g., bolometric maximum). However, 1D models miss important effects that are inherently multi-dimensional, such as mixing. We can mimic the impact of mixing in 1D by softening composition gradients, either artificially (e.g., Dessart et al. 2012a), or based on angular averages built from the few 3D simulations that exist, such as those of Gamezo, Khokhlov & Oran (2005). Performing multi-D radiative-transfer simulations would seem warranted but all such simulations so far have dramatically simplified the transfer (e.g., Kromer & Sim 2009). One should question if the gain in realism by going to 3D is not offset by the much simplified radiative transfer compared to 1D.

An argument often made is that a given explosion model, when post-processed by a radiative-transfer code, sometimes fails to reproduce a given observation. One can then propose that this initial explosion model is just not perfect. However, equally good interpretations are that the radiative-transfer is missing some important process, or that the atomic data is inaccurate. The advantage of our strategy over such targeted studies is that if a given mechanism is any good at reproducing SN Ia observations, we should be able to find a number of perfect matches — as we did. Out of a few hundred SNe Ia, some must be pointing the “right” way for our model, or have a suitable chemical stratification, i.e., so that what we adopt in our 1D model is a fair representation of what we see averaged over all viewing angles. A viable model can fail for one SN Ia, but should not fail for the few hundred SNe Ia for which we have data today.

With the same set of delayed-detonation models, we will now investigate the properties at earlier times (the brightening phase to the peak of the light curve) and later times (transition past the peak of the light curve into the nebular phase). Separately, we will perform similar simulations for a wider range of progenitor and explosion mechanisms, including pure deflagrations and pulsating delayed detonations.

ACKNOWLEDGMENTS

LD acknowledges financial support from the European Community through an International Re-integration Grant, under grant number PIRG04-GA-2008-239184. DJH acknowledges support from STScI theory grants HST-AR-11756.01.A and HST-AR-12640.01 and NASA theory grant NNX10AC80G. The work of AK was supported by the NSF grant AST-0709181 (A.K.) “Collaborative research: Three-Dimensional Simulations of Type Ia Supernovae: Constraining Models with Observations.” This work was granted access to the HPC resources of CINES under the allocation 2011-c2011046608 and 2012-c2012046608 made by GENCI (Grand Equipement National de Calcul Intensif). A subset of the computations were also performed at Caltech Center for Advanced Computing Research on the cluster Zwicky funded through NSF grant PHY-0960291 and the Sherman Fairchild Foundation. The

authors wish to thank: Eduardo Bravo for sending us his delayed-detonation model DDTc; Ryan Chornock, Alex Filippenko, and Jeff Silverman, for sending us spectra of SN 2007hj published by Silverman et al. (2012); Rubina Kotak, for sending us the spectrum of SN 2003gs used in this paper ahead of publication; Ivo Seitenzahl, for providing neutronization rates in machine-readable form. This research has made use of the CfA Supernova Archive, which is funded in part by the National Science Foundation through grant AST 0907903; the Online Supernova Spectrum Archive (SUSPECT); the Weizmann Interactive Supernova data Repository (WISEREP, Yaron & Gal-Yam 2012).

APPENDIX A: MODEL ATOMS

Table A1 gives the number of levels (both super-levels and full levels; see Hillier & Miller 1998 and Dessart & Hillier 2010 for details) for the model atoms used in the radiative-transfer calculations presented in this paper.

Oscillator strengths for CNO elements were originally taken from Nussbaumer & Storey (1983, 1984). These authors also provide transition probabilities to states in the ion continuum. The largest source of oscillator data is from Kurucz (2009)⁴; its principal advantage over many other sources (e.g., Opacity Project) is that LS coupling is not assumed. More recently, non-LS oscillator strengths have become available through the Iron Project (Hummer et al. 1993), and work done by the atomic-data group at Ohio State University (Nahar 2010). Other important sources of radiative data for Fe include Becker & Butler (1992, 1995a,b), Nahar (1995). Energy levels have generally been obtained from National Institute of Standards and Technology. Collisional data is sparse, particularly for states far from the ground state. The principal source for collisional data among low lying states for a variety of species is the tabulation by Mendoza (1983); other sources include Berrington et al. (1985), Lennon et al. (1985), Lennon & Burke (1994), Shine & Linsky (1974), Tayal (1997a,b), Zhang & Pradhan (1995a; 1995b; 1997). Photoionization data is taken from the Opacity Project (Seaton 1987) and the Iron Project (Hummer et al. 1993). Unfortunately Ni and Co photoionization data is generally unavailable, and we have utilized crude approximations. Charge exchange cross-sections are from the tabulation by Kingdon & Ferland (1996).

APPENDIX B: CONTRIBUTION OF INDIVIDUAL IONS TO THE TOTAL FLUX

In what follows we illustrate the contribution of individual ions to the full synthetic spectra, compared to the same observed SN Ia spectra as in Fig. 5. The upper pannel in each plot shows the full model (black) and the observed spectrum (red). Labels are the same as in Fig. 5. The lower pannel in each plot shows the contribution of individual ions, computed by taking the ratio of the full spectrum ($F_{\lambda, \text{All}}$) to that excluding all bound-bound transitions of the corresponding ion ($F_{\lambda, \text{less}}$).

We selected ions that contribute significantly to the observed total flux in at least one of the delayed-detonation models at bolometric maximum. The following ions showed essentially no noticeable contribution in the wavelength range considered here (2000–

Table A1. Summary of the model atoms used in our radiative-transfer calculations. The source of the atomic data sets is given in Dessart & Hillier (2010). N_f refers to the number of full levels, N_s to the number of super levels, and N_{trans} to the corresponding number of bound-bound transitions. The last column refers to the upper level for each ion treated. The total number of full (super) levels treated is 13 959 (2149), which corresponds to 629 396 bound-bound transitions. Note that nw^2W refers to a state with principal quantum number n (all l states combined into a single state), and spin 2. Similarly, $8z^1Z$ refers to the $n = 8$ state with high l states (usually $l = 4$ and above) combined and spin 1.

Species	N_f	N_s	N_{trans}	Upper Level
C I	26	14	120	2s2p ³ ³ P ^o
C II	26	14	87	2s ² 4d ² D _{5/2}
C III	112	62	891	2s8f ¹ F ^o
C IV	64	59	1446	$n = 30$
O I	51	19	214	2s ² 2p ³ (⁴ S ^o)4f ³ F ₃
O II	111	30	1157	2s ² 2p ² (³ P)4d ² D _{5/2}
O III	86	50	646	2p4f ¹ D
O IV	72	53	835	2p ² (³ P)3p ² P ^o
Ne I	139	70	1587	2s ² 2p ⁵ (² P ^o _{3/2})6d ² [5/2] _o
Ne II	91	22	1106	2s ² 2p ⁴ (³ P)4d ² P _{3/2}
Ne III	71	23	460	2s ² 2p ³ (² D ^o)3d ³ S ₁ ^o
Na I	71	22	1614	30w ² W
Mg II	65	22	1452	30w ² W
Mg III	99	31	775	2p ⁵ 7s ¹ P ^o
Al II	44	26	171	3s5d ¹ D ₂
Al III	45	17	362	10z ² Z
Si II	59	31	354	3s ² 7g ² G _{7/2}
Si III	61	33	310	3s5g ¹ G ₄
Si IV	48	37	405	10f ² F ^o
S II	324	56	8208	3s3p ³ (⁵ S ^o)4p ⁶ P
S III	98	48	837	3s3p ² (² D)3d ³ P
S IV	67	27	396	3s3p(³ P ^o)4p ² D _{5/2}
Ar I	110	56	1541	3s ² 3p ⁵ (² P ^o _{3/2})7p ² [3/2] ₂
Ar II	415	134	20197	3s ² 3p ⁴ (³ P ₁)7i ² [6] _{11/2}
Ar III	346	32	6898	3s ² 3p ³ (² D ^o)8s ¹ D ^o
Ca II	77	21	1736	3p ⁶ 30w ² W
Ca III	40	16	108	3s ² 3p ⁵ 5s ¹ P ^o
Ca IV	69	18	335	3s3p ⁵ (³ P ^o)3d ⁴ D _{1/2} ^o
Sc II	85	38	979	3p ⁶ 3d4f ¹ P ₁ ^o
Sc III	45	25	235	7h ² H _{11/2}
Ti II	152	37	3134	3d ² (³ F)5p ⁴ D _{7/2} ^o
Ti III	206	33	4735	3d6f ³ H ₆ ^o
Cr II	196	28	3629	3d ⁴ (³ G)4p x ⁴ G _{11/2} ^o
Cr III	145	30	2359	3d ³ (² D)4p ³ D ₃ ^o
Cr IV	234	29	6354	3d ² (³ P)5p ⁴ P _{5/2} ^o
Mn II	97	25	236	3d ⁴ (⁵ D)4s ² c ⁵ D ₄
Mn III	175	30	3173	3d ⁴ (³ G)4p y ⁴ H _{13/2} ^o
Fe I	136	44	1900	3d ⁶ (⁵ D)4s4p ⁵ F ₃ ^o
Fe II	827	275	44 831	3d ⁵ (⁶ S)4p ² (³ P) ⁴ P _{1/2}
Fe III	607	69	9794	3d ⁵ (⁴ D)6s ³ D ₂
Fe IV	1000	100	72 223	3d ⁴ (³ G)4f ⁴ P _{5/2} ^o
Fe V	191	47	3977	3d ³ (⁴ F)4d ⁵ F ₃
Fe VI	433	44	14 103	3p ⁵ (² P ^o)3d ⁴ (¹ S) ² P _{3/2} ^o
Co II	1000	81	61 986	3d ⁷ (⁴ P)4f ⁵ F ₄ ^o
Co III	1000	72	68 462	3d ⁶ (⁵ D)5f ⁴ F _{9/2} ^o
Co IV	1000	56	69 425	3d ⁵ (² D)5s ¹ D ₂
Co V	387	32	13 605	3d ⁴ (³ F)4d ² H _{9/2}
Co VI	323	28	9608	3d ³ (² D)4d ¹ S ₀
Ni II	1000	59	51 707	3d ⁸ (³ F)7f ⁴ I _{9/2}
Ni III	1000	47	66 486	3d ⁷ (² D)4d ³ S ₁ b
Ni IV	1000	54	72 898	3d ⁶ (⁵ D)6p ⁶ F _{11/2} ^o
Ni V	183	46	3065	3d ⁵ (² D)4p ³ F ₃ ^o
Ni VI	314	37	9569	3d ⁴ (⁵ D)4d ⁴ F _{9/2}

⁴ Data are available online at <http://kurucz.harvard.edu>

10000 Å): C I–II, O II, Ne II, Na I, Mg I, Al II–III, Ar III, Sc III, Ti III, Cr III, Mn II, and Ni III.

These plots are mostly for educational purposes, yet reveal key observed trends with decreasing ^{56}Ni mass: increase in Ca II strength (with double-absorption features resulting from optical-depth effects alone; see Sect. 5.4); increase of $\mathcal{R}(\text{Si})$ ratio and decrease of Si II 6355 Å absorption velocity and width; sudden onset of prominent Ti II/Sc II blanketing in the 4000–4500 Å region at the transition to low-luminosity SNe Ia; increase in strength of the O I 7773 Å line.

APPENDIX C: LOG OF BOLOMETRIC LUMINOSITY AND ABSOLUTE MAGNITUDES AT BOLOMETRIC MAXIMUM

Table C1 lists the bolometric luminosity and *UBVR IJHK* magnitudes of our models at bolometric maximum. The last line gives their standard deviation amongst our model series. Note the small scatter in the NIR bands with respect to the optical.

REFERENCES

- Altavilla G. et al., 2007, *A&A*, 475, 585
 Anders E., Grevesse N., 1989, *Geochim. Cosmochim. Acta*, 53, 197
 Arnett W. D., 1969, *Ap&SS*, 5, 180
 —, 1979, *ApJ*, 230, L37
 —, 1982, *ApJ*, 253, 785
 Badenes C., Borkowski K. J., Hughes J. P., Hwang U., Bravo E., 2006, *ApJ*, 645, 1373
 Badenes C., Hughes J. P., Cassam-Chenaï G., Bravo E., 2008, *ApJ*, 680, 1149
 Baron E., Hauschildt P. H., Nugent P., Branch D., 1996, *MNRAS*, 283, 297
 Baron E., Höflich P., Krisciunas K., Dominguez I., Khokhlov A. M., Phillips M. M., Suntzeff N., Wang L., 2012, *ApJ*, 753, 105
 Becker S. R., Butler K., 1992, *A&A*, 265, 647
 —, 1995a, *A&A*, 294, 215
 —, 1995b, *A&A*, 301, 187
 Benetti S. et al., 2004, *MNRAS*, 348, 261
 Berrington K. A., Burke P. G., Dufton P. L., Kingston A. E., 1985, *Atomic Data and Nuclear Data Tables*, 33, 195
 Blondin S., Kasen D., Röpke F. K., Kirshner R. P., Mandel K. S., 2011, *MNRAS*, 417, 1280
 Blondin S. et al., 2012, *AJ*, 143, 126
 Blondin S., Prieto J. L., Patat F., Challis P., Hicken M., Kirshner R. P., Matheson T., Modjaz M., 2009, *ApJ*, 693, 207
 Blondin S., Tonry J. L., 2007, *ApJ*, 666, 1024
 Branch D., Buta R., Falk S. W., McCall M. L., Uomoto A., Wheeler J. C., Wills B. J., Sutherland P. G., 1982, *ApJ*, 252, L61
 Branch D. et al., 2006, *PASP*, 118, 560
 Bravo E., García-Senz D., 1999, *MNRAS*, 307, 984
 Brown P. J. et al., 2010, *ApJ*, 721, 1608
 Bufano F. et al., 2009, *ApJ*, 700, 1456
 Colgate S. A., McKee C., 1969, *ApJ*, 157, 623
 Dessart L., Hillier D. J., 2005, *A&A*, 437, 667
 —, 2008, *MNRAS*, 383, 57
 —, 2010, *MNRAS*, 405, 2141
 Dessart L., Hillier D. J., Li C., Woosley S., 2012a, *MNRAS*, 424, 2139
 Dessart L., Hillier D. J., Waldman R., Livne E., Blondin S., 2012b, *MNRAS*, 426, L76
 Fesen R. A., Höflich P. A., Hamilton A. J. S., Hammell M. C., Gerardy C. L., Khokhlov A. M., Wheeler J. C., 2007, *ApJ*, 658, 396
 Filippenko A. V. et al., 1992, *AJ*, 104, 1543
 Folatelli G. et al., 2012, *ApJ*, 745, 74
 Foley R. J. et al., 2012, *ApJ*, 744, 38
 Fowler W. A., Woosley S. E., Engelbrecht C. A., 1978, *ApJ*, 226, 984
 Gamezo V. N., Khokhlov A. M., Oran E. S., 2005, *ApJ*, 623, 337
 Gamezo V. N., Khokhlov A. M., Oran E. S., Chtchelkanova A. Y., Rosenberg R. O., 2003, *Science*, 299, 77
 Garavini G. et al., 2005, *AJ*, 130, 2278
 —, 2007, *A&A*, 471, 527
 Garnavich P. M. et al., 2004, *ApJ*, 613, 1120
 Hachinger S., Mazzali P. A., Tanaka M., Hillebrandt W., Benetti S., 2008, *MNRAS*, 389, 1087
 Hamuy M. et al., 2002, *AJ*, 124, 417
 Hillier D. J., Dessart L., 2012, *MNRAS*, 3136
 Hillier D. J., Müller D. L., 1998, *ApJ*, 496, 407
 Höflich P., Gerardy C. L., Fesen R. A., Sakai S., 2002, *ApJ*, 568, 791
 Höflich P., Khokhlov A., 1996, *ApJ*, 457, 500
 Höflich P., Khokhlov A. M., Wheeler J. C., 1995, *ApJ*, 444, 831
 Höflich P. et al., 2010, *ApJ*, 710, 444
 Höflich P., Müller E., Khokhlov A., 1993, *A&A*, 268, 570
 Höflich P., Wheeler J. C., Thielemann F. K., 1998, *ApJ*, 495, 617
 Howell D. A., Höflich P., Wang L., Wheeler J. C., 2001, *ApJ*, 556, 302
 Hoyle F., Fowler W. A., 1960, *ApJ*, 132, 565
 Hummer D. G., Berrington K. A., Eissner W., Pradhan A. K., Saraph H. E., Tully J. A., 1993, *A&A*, 279, 298
 Iben, Jr. I., Tutukov A. V., 1984, *ApJS*, 54, 335
 Jack D., Hauschildt P. H., Baron E., 2009, *A&A*, 502, 1043
 Kasen D., 2006, *ApJ*, 649, 939
 Kasen D., Röpke F. K., Woosley S. E., 2009, *Nature*, 460, 869
 Kasen D., Thomas R. C., Nugent P., 2006, *ApJ*, 651, 366
 Khokhlov A., Müller E., Höflich P., 1993, *A&A*, 270, 223
 Khokhlov A. M., 1991, *A&A*, 245, 114
 Kingdon J. B., Ferland G. J., 1996, *ApJS*, 106, 205
 Kirshner R. P. et al., 1993, *ApJ*, 415, 589
 Kozma C., Fransson C., Hillebrandt W., Travaglio C., Sollerman J., Reinecke M., Röpke F. K., Spyromilio J., 2005, *A&A*, 437, 983
 Krisciunas K. et al., 2012, arXiv:1211.1362
 —, 2009, *AJ*, 138, 1584
 Krisciunas K., Phillips M. M., Suntzeff N. B., 2004, *ApJ*, 602, L81
 Kromer M., Sim S. A., 2009, *MNRAS*, 398, 1809
 Kurucz R. L., 2009, in *American Institute of Physics Conference Series*, Vol. 1171, American Institute of Physics Conference Series, Hubeny I., Stone J. M., MacGregor K., Werner K., eds., pp. 43–51
 Leibundgut B. et al., 1993, *AJ*, 105, 301
 Lennon D. J., Burke V. M., 1994, *A&AS*, 103, 273
 Lennon D. J., Dufton P. L., Hibbert A., Kingston A. E., 1985, *ApJ*, 294, 200
 Lentz E. J., Baron E., Branch D., Hauschildt P. H., Nugent P. E., 2000, *ApJ*, 530, 966

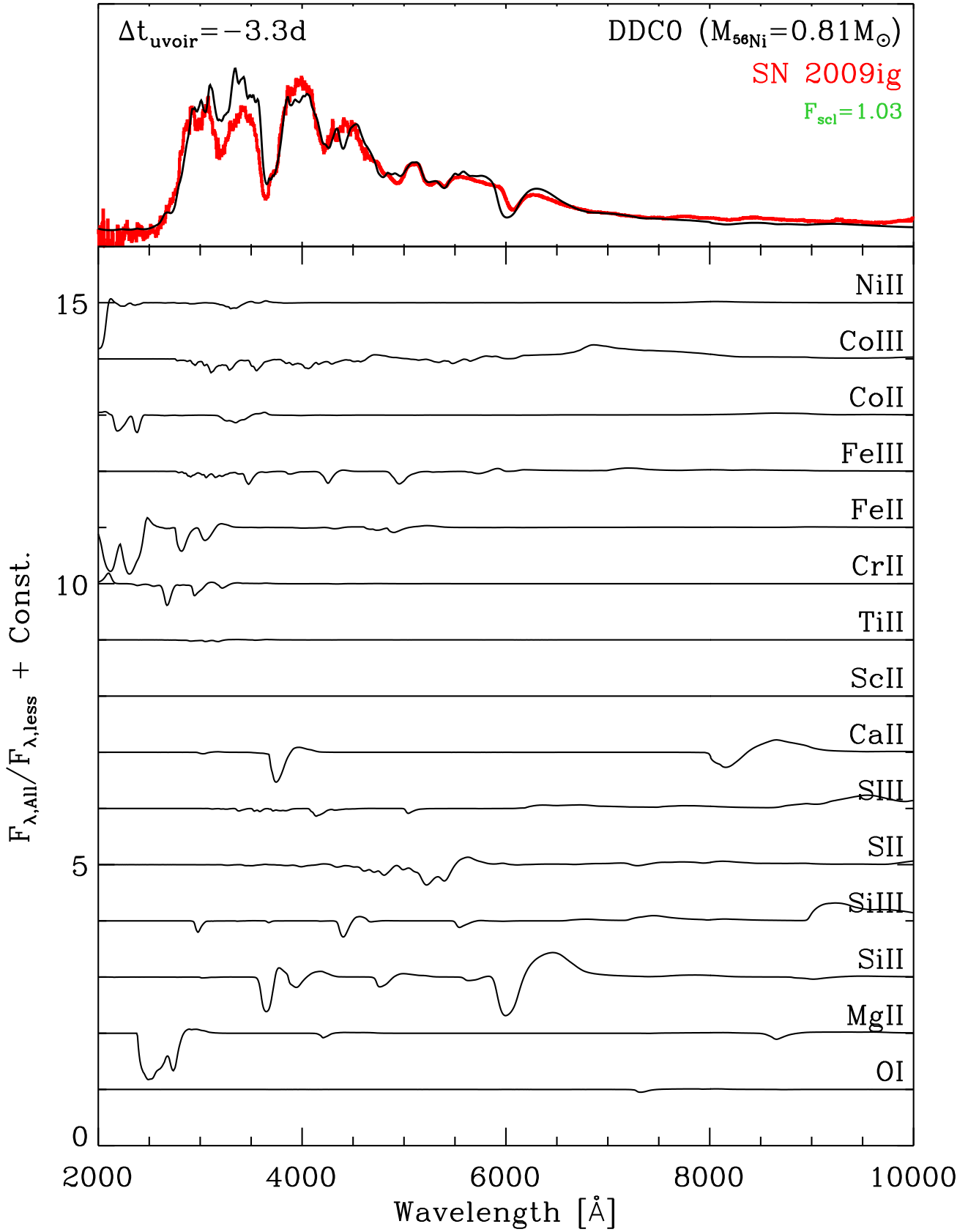


Figure B1. Contribution of individual ions (bottom) to the full synthetic spectrum of DDC0 (top, black line), compared to SN 2009ig at -3.3 d from UVOIR maximum (top, red line).

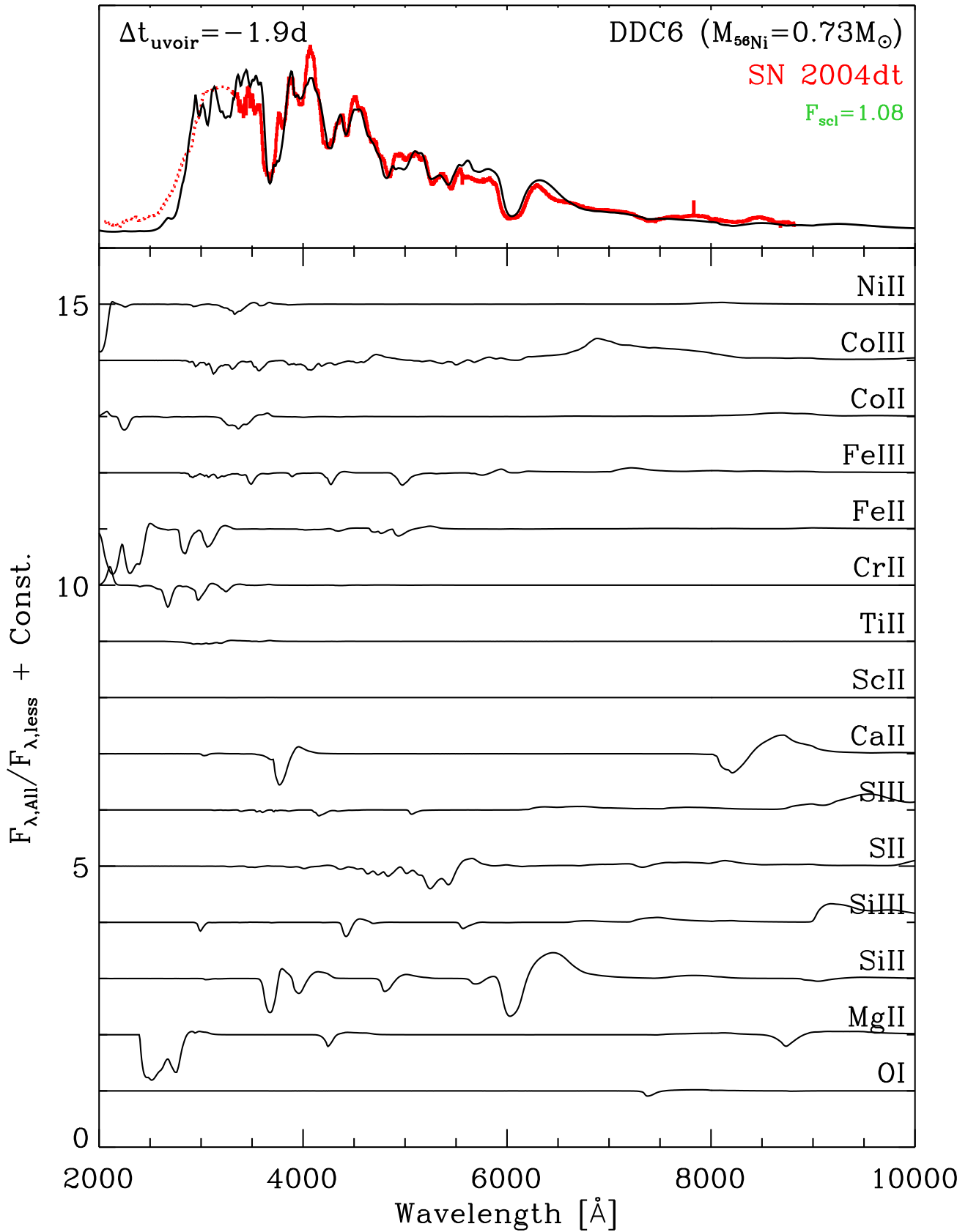


Figure B2. Contribution of individual ions (bottom) to the full synthetic spectrum of DDC6 (top, black line), compared to SN 2004dt at -1.9d from UVOIR maximum (top, red line).

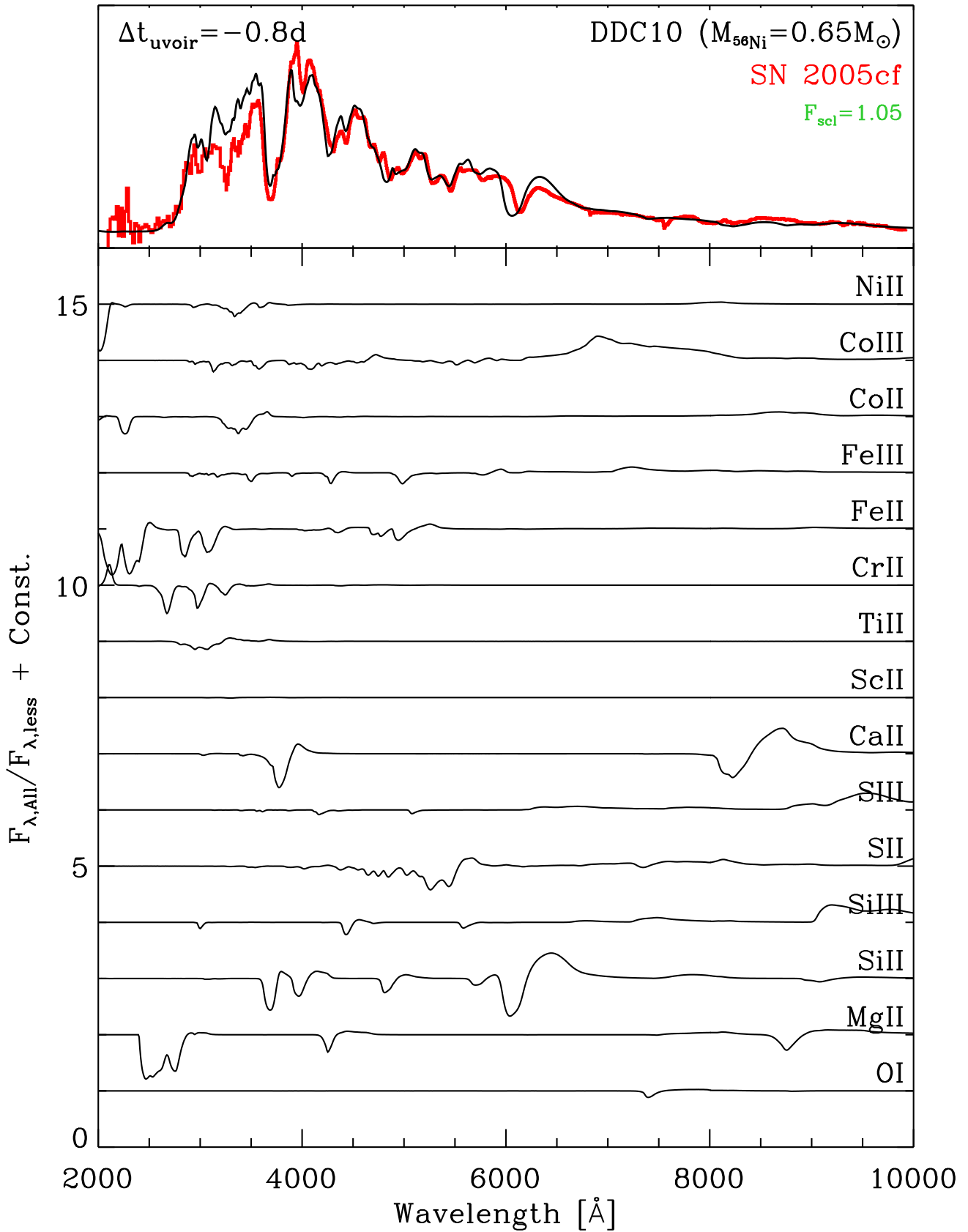


Figure B3. Contribution of individual ions (bottom) to the full synthetic spectrum of DDC10 (top, black line), compared to SN 2005cf at -0.8 d from UVOIR maximum (top, red line).

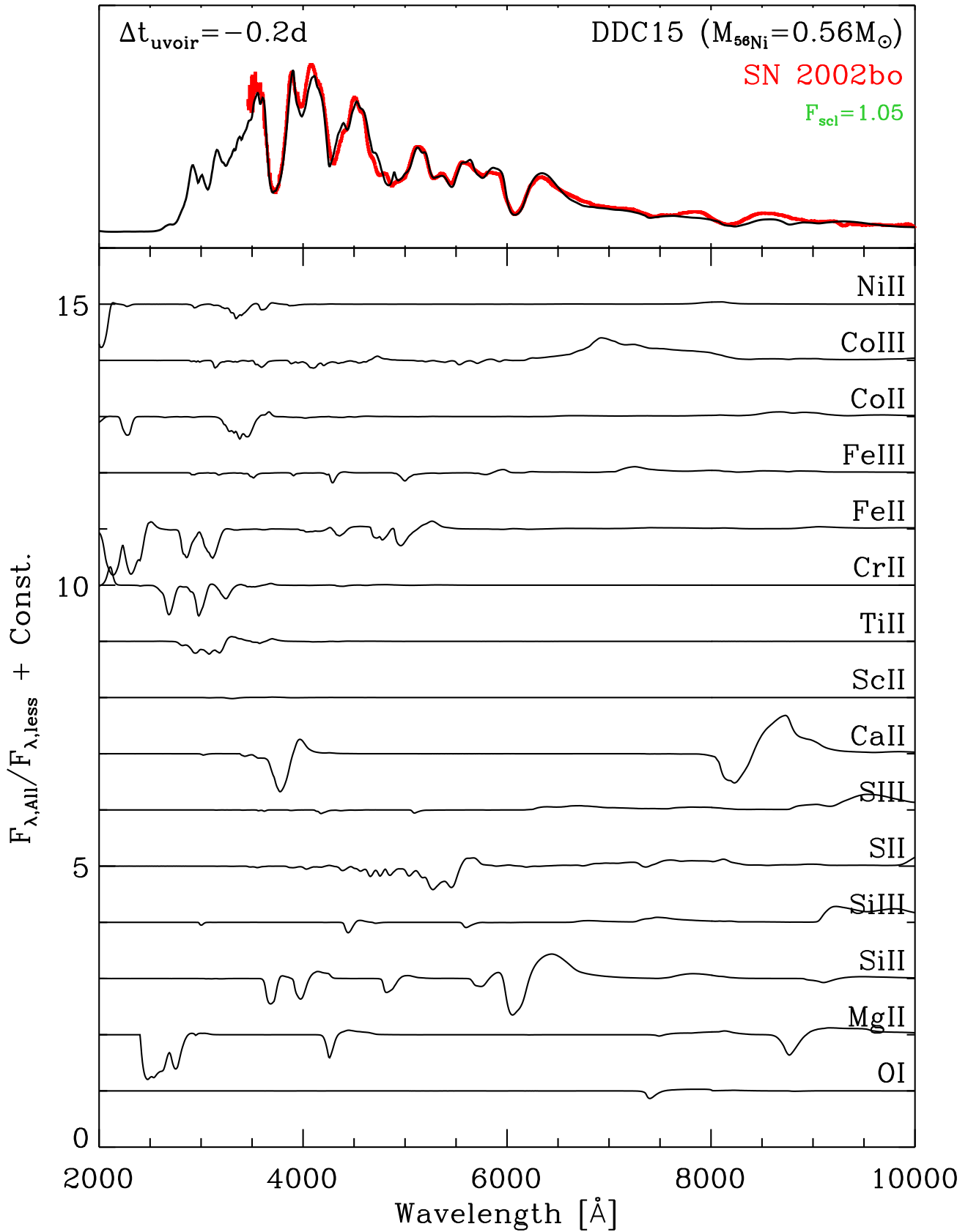


Figure B4. Contribution of individual ions (bottom) to the full synthetic spectrum of DDC15 (top, black line), compared to SN 2002bo at -0.2 d from UVOIR maximum (top, red line).

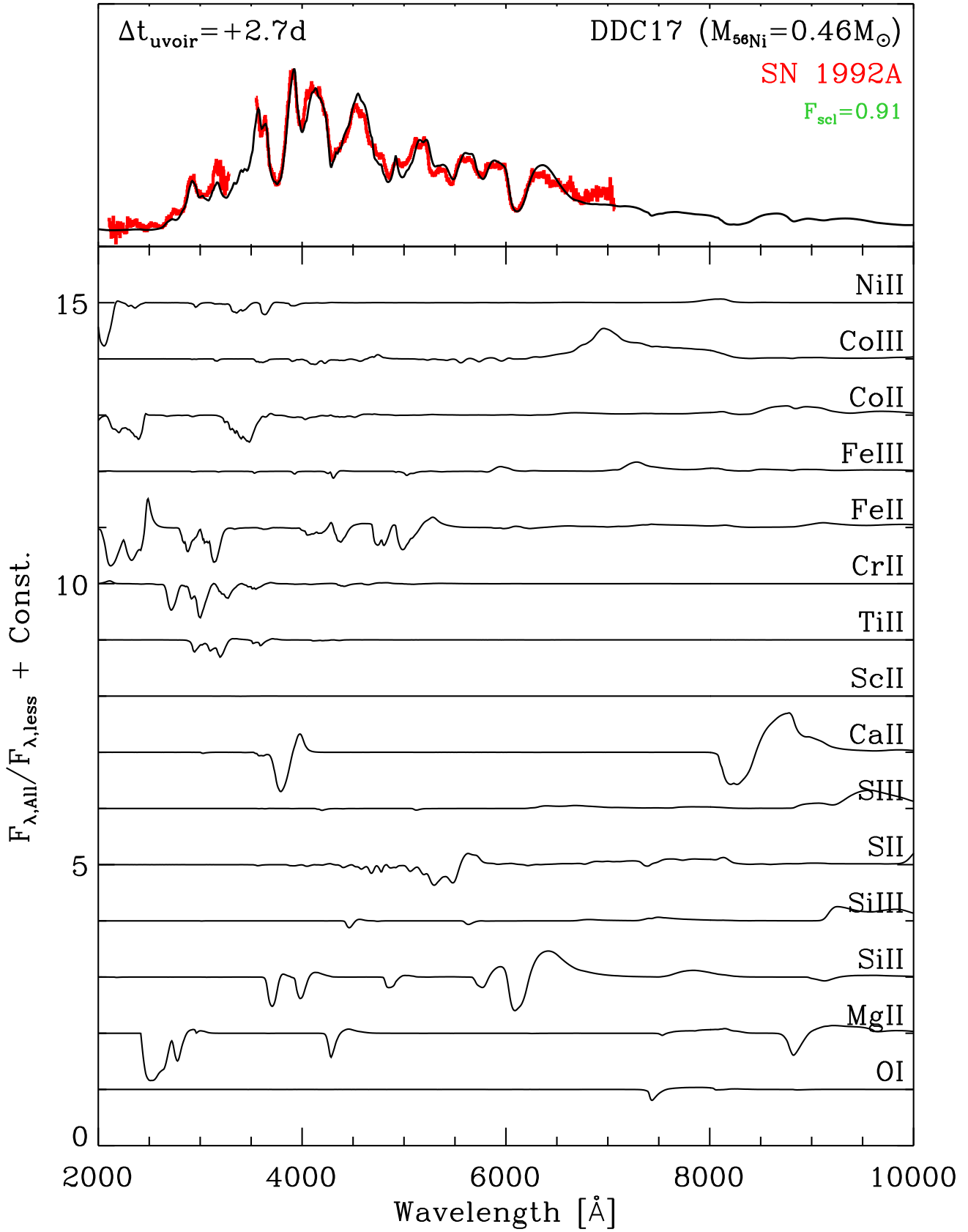


Figure B5. Contribution of individual ions (bottom) to the full synthetic spectrum of DDC17 (top, black line), compared to SN 1992A at +2.7 d from UVOIR maximum (top, red line).

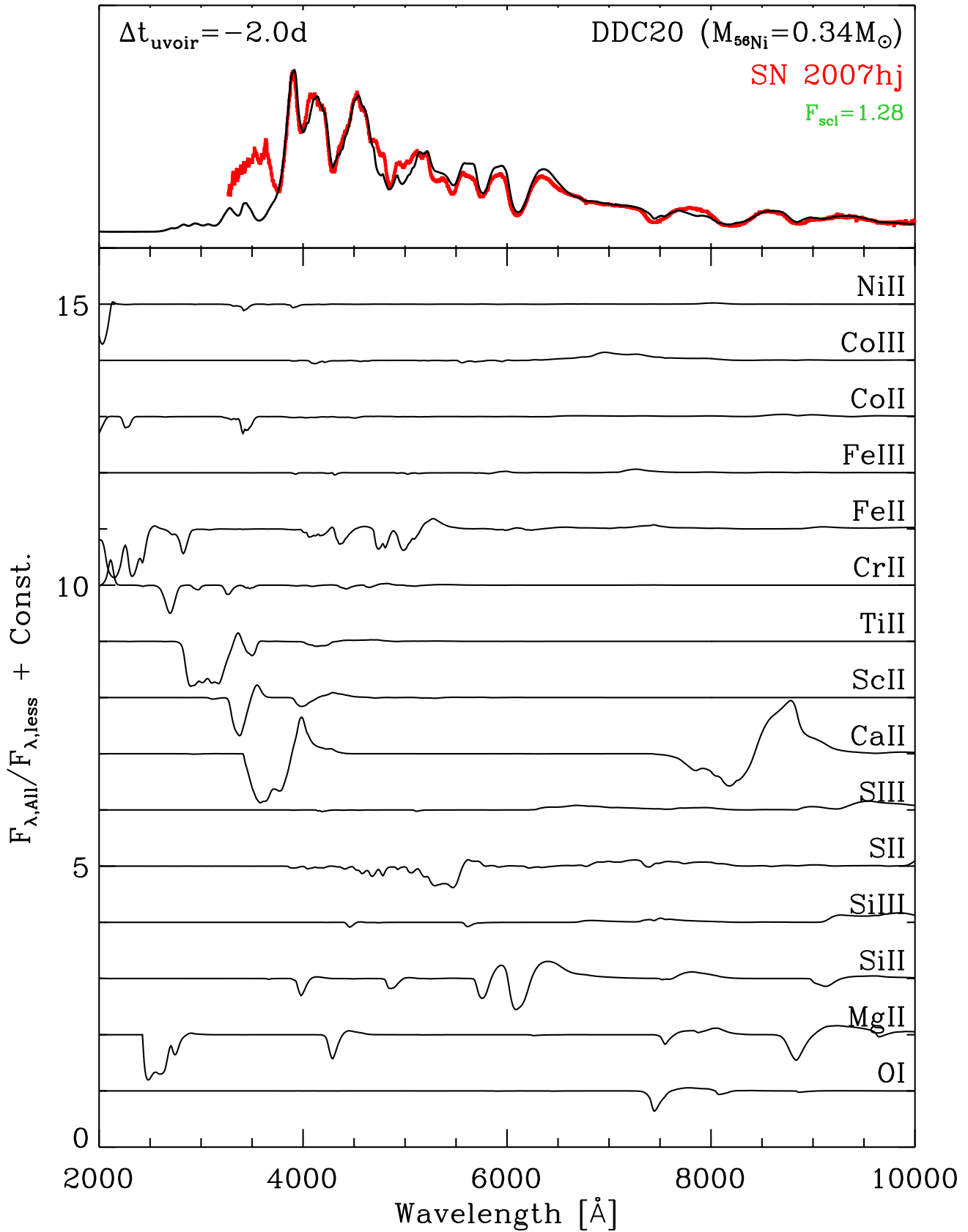


Figure B6. Contribution of individual ions (bottom) to the full synthetic spectrum of DDC20 (top, black line), compared to SN 2007hj at -2.0 d from UVOIR maximum (top, red line).

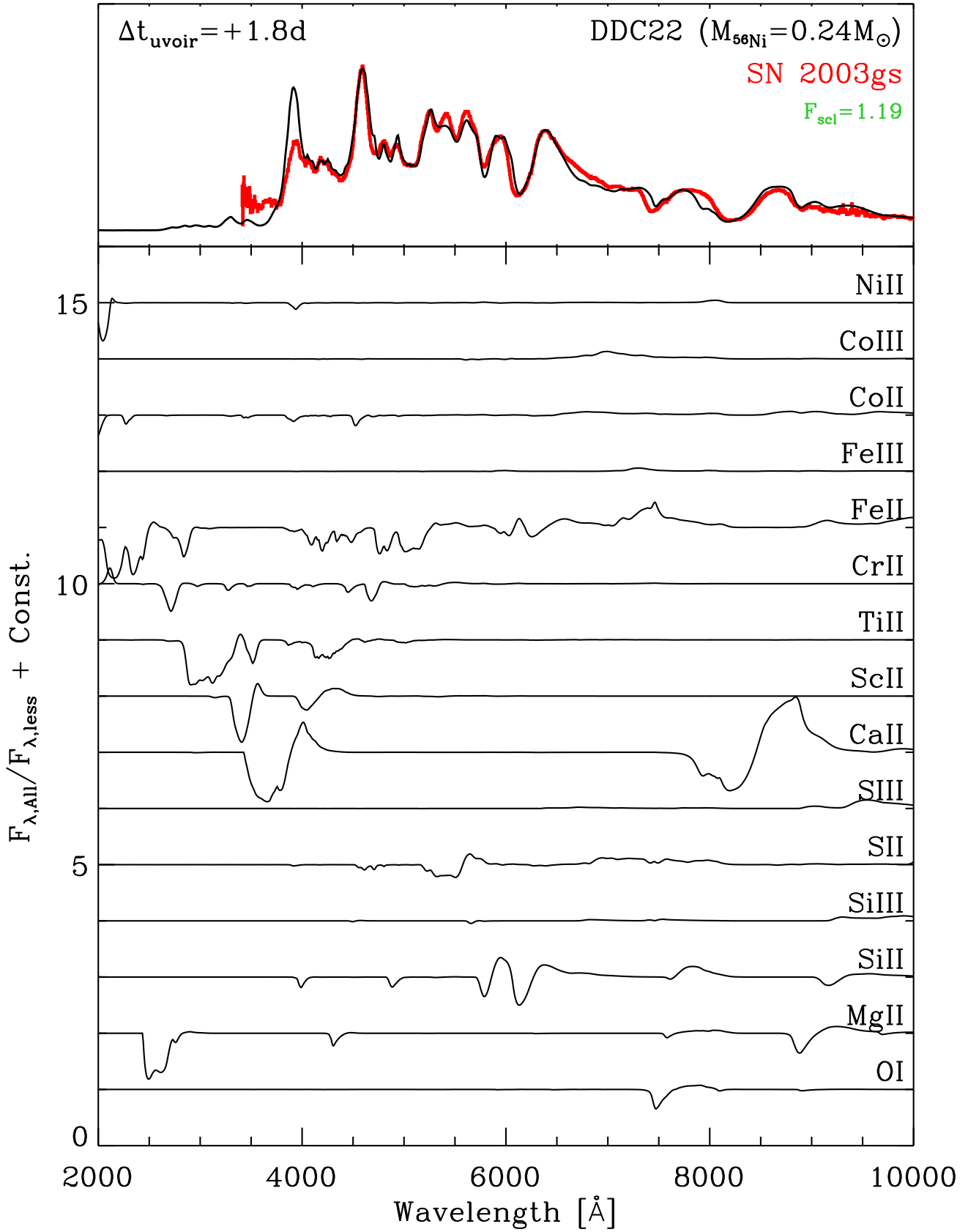


Figure B7. Contribution of individual ions (bottom) to the full synthetic spectrum of DDC22 (top, black line), compared to SN 2003gs at +1.8d from UVOIR maximum (top, red line).

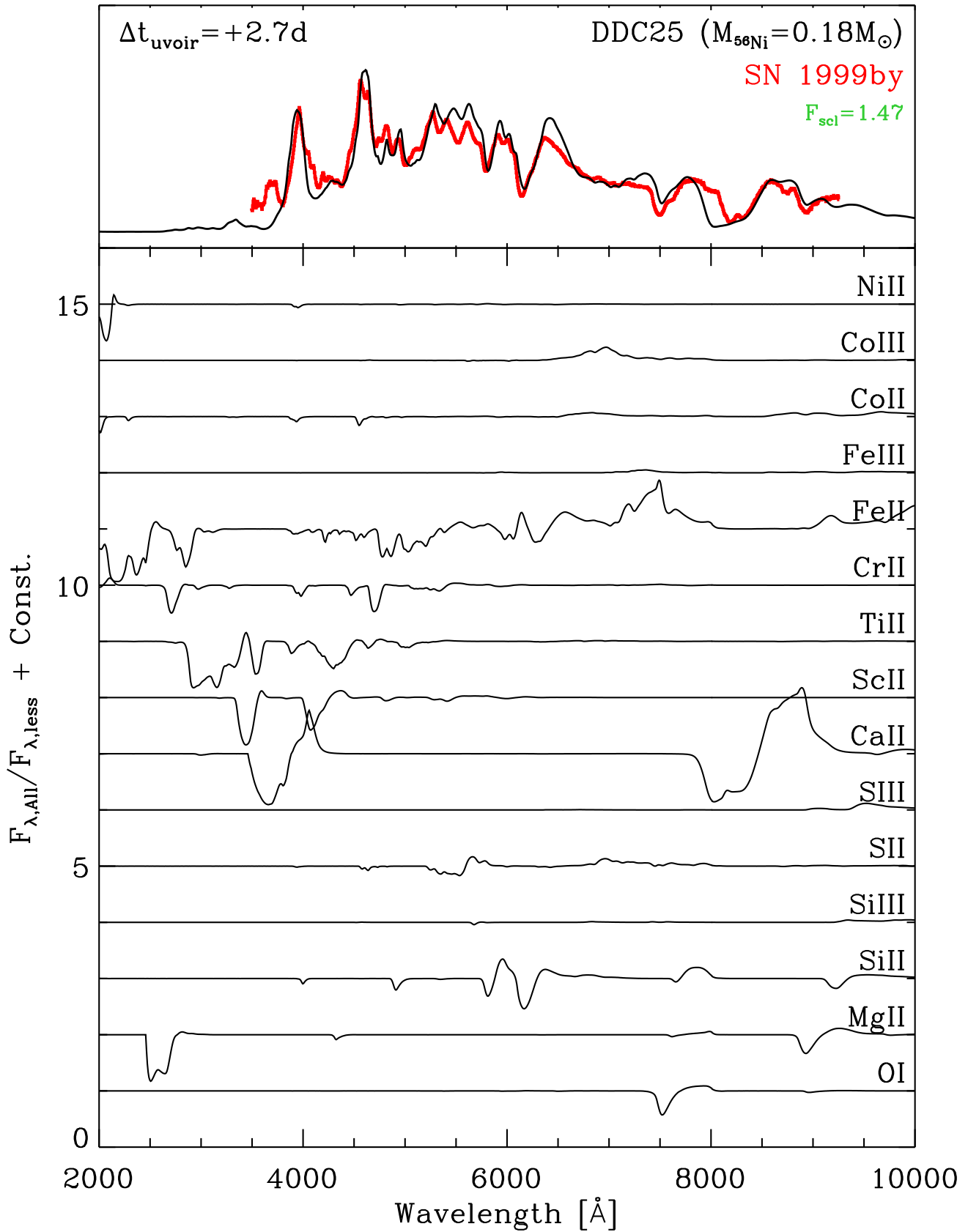


Figure B8. Contribution of individual ions (bottom) to the full synthetic spectrum of DDC25 (top, black line), compared to SN 1999by at +2.7 d from UVOIR maximum (top, red line).

Table C1. Bolometric luminosity and absolute *UBVRIJHK* magnitudes at bolometric maximum in our model set.

Model	L_{bol} [erg s ⁻¹]	M_U [mag]	M_B [mag]	M_V [mag]	M_R [mag]	M_I [mag]	M_J [mag]	M_H [mag]	M_K [mag]
DDC0	1.77(43)	-20.16	-19.53	-19.51	-19.36	-18.67	-18.14	-17.41	-17.56
DDC6	1.62(43)	-20.05	-19.44	-19.41	-19.31	-18.66	-18.18	-17.44	-17.52
DDC10	1.45(43)	-19.91	-19.35	-19.30	-19.26	-18.69	-18.26	-17.54	-17.56
DDC15	1.22(43)	-19.63	-19.20	-19.16	-19.18	-18.73	-18.33	-17.68	-17.64
DDC17	1.03(43)	-19.28	-19.03	-19.03	-19.09	-18.70	-18.33	-17.78	-17.67
DDC20	7.65(42)	-18.42	-18.75	-18.84	-18.91	-18.61	-18.34	-17.99	-17.78
DDC22	5.10(42)	-17.34	-17.99	-18.51	-18.64	-18.47	-18.28	-18.17	-17.90
DDC25	3.64(42)	-16.65	-17.40	-18.19	-18.36	-18.20	-18.07	-18.04	-17.72
StdDev	5.16(42)	1.33	0.76	0.46	0.35	0.18	0.10	0.29	0.13

Note: Numbers in parentheses correspond to powers of ten.

Li C., Hillier D. J., Dessart L., 2012, *MNRAS*, 426, 1671
 Macri L. M., Stetson P. B., Bothun G. D., Freedman W. L., Gar-
 navich P. M., Jha S., Madore B. F., Richmond M. W., 2001, *ApJ*,
 559, 243
 Mandel K. S., Narayan G., Kirshner R. P., 2011, *ApJ*, 731, 120
 Matheson T. et al., 2008, *AJ*, 135, 1598
 Mazzali P. A. et al., 2005, *ApJ*, 623, L37
 Mazzali P. A., Lucy L. B., 1993, *A&A*, 279, 447
 Mazzali P. A., Sauer D. N., Pastorello A., Benetti S., Hillebrandt
 W., 2008, *MNRAS*, 386, 1897
 Mendoza C., 1983, in *IAU Symposium*, Vol. 103, Planetary Neb-
 ulae, D. R. Flower, ed., pp. 143–172
 Milne P. A. et al., 2010, *ApJ*, 721, 1627
 Nahar S. N., 1995, *A&A*, 293, 967
 —, 2010, *Norad-atomic-data*
 Nomoto K., Sugimoto D., Neo S., 1976, *Ap&SS*, 39, L37
 Nugent P., Phillips M., Baron E., Branch D., Hauschildt P., 1995,
ApJ, 455, L147+
 Nugent P. E. et al., 2011, *Nature*, 480, 344
 Nussbaumer H., Storey P. J., 1983, *A&A*, 126, 75
 —, 1984, *A&AS*, 56, 293
 Pakmor R., Hachinger S., Röpke F. K., Hillebrandt W., 2011,
A&A, 528, A117+
 Pakmor R., Kromer M., Röpke F. K., Sim S. A., Ruiter A. J., Hille-
 brandt W., 2010, *Nature*, 463, 61
 Pakmor R., Kromer M., Taubenberger S., Sim S. A., Röpke F. K.,
 Hillebrandt W., 2012, *ApJ*, 747, L10
 Parrent J. T. et al., 2011, *ApJ*, 732, 30
 Pastorello A. et al., 2007, *MNRAS*, 377, 1531
 Phillips M. M., 1993, *ApJ*, 413, L105
 Phillips M. M. et al., 2006, *AJ*, 131, 2615
 Pignata G. et al., 2008, *MNRAS*, 388, 971
 Pinto P. A., Eastman R. G., 2000a, *ApJ*, 530, 744
 —, 2000b, *ApJ*, 530, 757
 Pskovskii I. P., 1977, *Soviet Astronomy*, 21, 675
 Röpke F. K. et al., 2012, *ApJ*, 750, L19
 Röpke F. K., Niemeyer J. C., 2007, *A&A*, 464, 683
 Sauer D. N. et al., 2008, *MNRAS*, 391, 1605
 Schlegel D. J., Finkbeiner D. P., Davis M., 1998, *ApJ*, 500, 525
 Seaton M. J., 1987, *Journal of Physics B Atomic Molecular*
Physics, 20, 6363
 Seitenzahl I. R., Townsley D. M., Peng F., Truran J. W., 2009,
Atomic Data and Nuclear Data Tables, 95, 96
 Shine R. A., Linsky J. L., 1974, *Sol. Phys.*, 39, 49
 Silverman J. M., Filippenko A. V., 2012, *MNRAS*, 425, 1917
 Silverman J. M. et al., 2012, *MNRAS*, 425, 1789
 Sim S. A., 2007, *MNRAS*, 375, 154
 Sim S. A., Röpke F. K., Hillebrandt W., Kromer M., Pakmor R.,
 Fink M., Ruiter A. J., Seitenzahl I. R., 2010, *ApJ*, 714, L52
 Taubenberger S. et al., 2008, *MNRAS*, 385, 75
 Tayal S. S., 1997a, *ApJS*, 111, 459
 —, 1997b, *ApJ*, 481, 550
 Thomas R. C. et al., 2011, *ApJ*, 743, 27
 Travaglio C., Hillebrandt W., Reinecke M., Thielemann F., 2004,
A&A, 425, 1029
 Tully R. B., Fisher J. R., 1988, *Catalog of Nearby Galaxies*
 Utrobin V. P., Chugai N. N., 2005, *A&A*, 441, 271
 Valenti S. et al., 2008, *MNRAS*, 383, 1485
 Wang L. et al., 2003, *ApJ*, 591, 1110
 Wang X. et al., 2009a, *ApJ*, 699, L139
 —, 2009b, *ApJ*, 697, 380
 —, 2012, *ApJ*, 749, 126
 Webbink R. F., 1984, *ApJ*, 277, 355
 Whelan J., Iben I. J., 1973, *ApJ*, 186, 1007
 Wood-Vasey W. M. et al., 2008, *ApJ*, 689, 377
 Woosley S. E., 1991, in *American Institute of Physics Conference*
Series, Vol. 232, Gamma-Ray Line Astrophysics, Durouchoux
 P., Prantzos N., eds., pp. 270–290
 Woosley S. E., Fowler W. A., Holmes J. A., Zimmerman B. A.,
 1978, *Atomic Data and Nuclear Data Tables*, 22, 371
 Woosley S. E., Kasen D., Blinnikov S., Sorokina E., 2007, *ApJ*,
 662, 487
 Yaron O., Gal-Yam A., 2012, *PASP*, 124, 668
 Zhang H. L., Pradhan A. K., 1995a, *A&A*, 293, 953
 —, 1995b, *Journal of Physics B Atomic Molecular Physics*, 28,
 3403
 —, 1997, *A&AS*, 126, 373